

ADH 035820



DDC  
RECORDED  
JAN 21 1977  
SERIALIZED

# PRATT & WHITNEY AIRCRAFT

East Hartford, Connecticut 06108

25 October 1976

In reply please refer to  
MJB:DA:EB - J Mezz

To: Air Force Materials Laboratory (FY 7615)  
Attn: AFML/LLS  
Wright-Patterson AFB, Ohio 45433

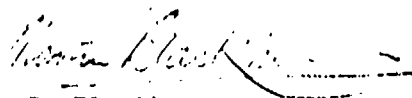
Subject: Subsurface Defects in Wrought Titanium Alloy -  
Third Semi-Annual Report

Reference: Contract F33615-75-C-5138, Project 7353

Enclosures: a. Five Copies of Report  
b. One Reproducible

Six copies of the subject report are submitted herewith to fulfill the requirements of Item No. 0002, Sequence No. A002 in the referenced contract.

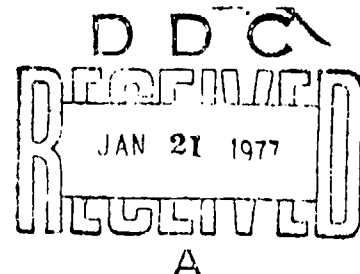
UNITED TECHNOLOGIES CORPORATION  
Pratt & Whitney Aircraft Division

  
M. J. Blackburn  
Program Manager

Transmittal Letter Only:

USAF/AFSC  
4950th Test Wing (FQ 8419)  
Wright-Patterson AFB, Ohio 45433

Naval Plant Representative Office  
Pratt & Whitney Aircraft  
East Hartford, Connecticut 06108



①

INFLUENCE OF SUBSURFACE DEFECTS  
ON FATIGUE PROPERTIES OF TITANIUM ALLOYS

Covering Period April 1976 - October 1976

114 25 Oct 1976

12-004.1

Prepared For

*J. J. ...*

Materials and Ceramics Laboratory  
Wright-Patterson Air Force Base, Ohio



Prepared by

C.C. Law M.J. Blackburn  
Materials Engineering and Research Laboratory  
East Hartford, Connecticut

**PRATT & WHITNEY AIRCRAFT**



Division of  
**UNITED  
TECHNOLOGIES**

EAST HARTFORD, CONNECTICUT

114 PW  
REF. NO. 75-200-4017-8

COPY NO.

D D C  
RECEIVED  
JAN 21 1977  
REGISTERED

**DISTRIBUTION STATEMENT A**  
Approved for public release;  
Distribution Unlimited

TABLE OF CONTENTS

	<u>PAGE</u>
A. Introduction	1
B. Cleavage Rosette Failures	2
I. Introduction	2
II. Experimental	2
i. Fabrication and Testing of Diffusion Bonded Specimens with Seeded Contaminants	2
ii. Chemistry Determination on Rosette Defects	3
III. Results	4
i. LCF Testing of IMI 685 Specimens	4
1. Defect-Free Material	4
2. Defective Material	4
3. Seeded (Defective) Material	5
ii. Chemistry Determination on Rosette Defects	6
1. IMI 685 Specimen #4	6
2. Thermomechanically Processed Specimen	7
iii. LCF Testing of Seeded Specimens from Other $\alpha$ - $\beta$ Ti Alloys	8
IV. Discussion	9
i. Fractographic Features	10
ii. The Fatigue Debits in IMI 685	11
iii. Seeded Specimens of Other $\alpha$ - $\beta$ Ti Alloys	13
References	15
Tables	16-19
Figure Captions	20-21

	<u>PAGE</u>
C. Beta Flack Defects	41
I. Introduction	41
II. Experimental	41
i. Specimen Fabrication and Testing	41
ii. Residual Stress Determination	42
iii. Chemistry Determination by Secondary Ion Mass Spectrometry	43
III. Results	43
i. LCF Properties of Ti-6Al-4V	43
1. Surface Residual Stress Effects	43
2. The Influence of Test Conditions	44
ii. Residual Stress Measurements	44
iii. Secondary Ion Mass Spectrometry Measurements	45
IV. Discussion	45
References	47
Tables	48-49
Figure Captions	50

ACCESSION INFO	
NTIS	WHIS SERIALIZED ✓
DDC	WHIS SERIALIZED
UNCLASSIFIED	
JUSTIFICATION	
<i>Butler on 6/10</i>	
BY	DISTRIBUTION, AVAILABILITY OFFICE
DATE	ANAL. DIV. CONTROL
A	

A. INTRODUCTION

This report summarizes work performed in the third six months of Contract Number AF33615-75-5138 in which the influence of specific defects on the properties of titanium alloys is studied in order to provide insight into the origin and reason for the property modifications.

Few manufacturing processes are perfect and errors, minor changes in a processing cycle, etc., can lead to defective regions in a product which may influence service performance. Such defects can take many forms; for example, voids, chemical segregation, inclusions, etc., and can influence both mechanical and physical properties. However, it is clear that the main problems encountered in service have been in the degradation of fatigue properties. Over the past decades the demands of high technology areas such as these in the aerospace industry have required that such defects be eliminated from components and the advances in quality control, NDI, etc., have proved in general very successful in improving product integrity. Titanium alloys have formed part of such programs and the service record of these materials has been excellent indicating that the techniques for controlling defects have been, on the whole, very successful. However, occasional problems have been encountered especially when the defects occur on a small scale and are difficult to detect by NDI techniques. It would be fair to state that solutions to such problems have been found relatively soon after identification but the reasons behind the modification of properties produced by such defects are less well understood. Description of the types of defects that have been encountered were identified in the first semi-annual report. This has been used to establish an experimental and analytical program designed to gain insight into the nature and effect of two specific defects on subsequent mechanical properties.

These two defects are, firstly small discontinuities that under cyclic loading lead to rapid nucleation and growth of cracks. The appearance of the fatigue fracture surface has led to the term 'cleavage rosette' to describe the failure characteristics. The second defect is the better characterized structural discontinuity that occurs in alpha beta processed titanium alloys and termed beta fleck. The major influence of these defects are on the fatigue properties of the material. ←

## B. CLEAVAGE ROSETTE FAILURES

### I. INTRODUCTION

During this reporting period the cleavage rosette problem has been studied by two approaches. Firstly, LCF life, crack growth results and fractographic data generated by Rolls Royce<sup>(1)</sup>, the Air Force/Metcut<sup>(2)</sup> and Pratt & Whitney were collected and analyzed to better define the magnitude of the fatigue debit and possibly provide insight into the reasons for such a debit. The second approach the LCF and fractographic features of specimens which had been seeded with various types of contaminants were studied to determine whether the characteristics of rosette-type failure could be reproduced. In contrast to previous work (see the 1st Annual Report) these seeded specimens were beta heat treated after diffusion bonding to produce an acicular microstructure similar to that of the IMI 685 alloy.

### II. EXPERIMENTAL

#### 1. Fabrication and Testing of Diffusion Bonded Specimens with Seeded Contaminants.

Three groups of specimens have been fabricated and tested. The first group consists of IMI 685 specimens machined from a relatively defect-free region of the forging. These specimens were seeded with either a .03" diagonal hardness indentation (simulated pore) or an indentation containing Ti-6Al-4V hydride (simulation of a contaminated pore). The seeded IMI 685 specimens were all tested at a maximum stress of 110 KSI at either R = 0, 20 cpm, or R = 0.3, 12 cph. The microstructure of these specimens after diffusion bonding were essentially the same as that in the forging.

The second and third group of specimens were fabricated from  $\alpha$ - $\beta$  forged Ti-6Al-4V and Ti-6Al-2Sn-4Zr-2Mo alloys respectively.

The second group of specimens were seeded either with a 0.30" diagonal hardness indentation or an indentation containing one of the following contaminants: Ti-6Al-4V hydride, NaCl, TiN and Al. The specimen fabrication procedures for the first and second groups were the same as those described in the first Semi-Annual Report except that the diffusion bonding conditions were changed slightly to minimize the amount of plastic deformation during diffusion bonding. This results in less displacement of the seeded flaw and easier location in a fabricated test specimen. The bonding conditions for the first and second groups are, respectively, 1800°F/500 psi/4 hours and 1650°F/800 psi/4 hours.

The third group of specimens were seeded with argon. Figure 1 illustrates the configuration used for trapping argon in the pore. One half of the specimen has a ball radius at one end which is in contact with a pore in one end of the second half of the specimen. The specimen halves were assembled in an argon atmosphere, load was then applied and the temperature increased. The plastic deformation in the contact ends helps to seal the argon in the pore while the curvature limits the argon trapped at the interface. Ideally, the argon should be evacuated as soon as the pore has been sealed. Since the condition for adequate sealing cannot be readily determined, argon was evacuated at two arbitrarily selected temperatures either 200°F or 800°F. The diffusion bonding was performed initially at 1750°F/500 psi/4 hours but subsequently changed to 1850°F/560 psi/4 hours.

After diffusion bonding, these specimens were given a beta heat treatment of 2000°F for 1 hour followed by furnace cooling. The heat treated specimens were tested at 0-110 ksi, 1 cpm.

#### ii. Chemistry Determination on Rosette Defects

Two different techniques for chemically analyzing defects have been attempted. The simplest method was to produce rosette-type of failure and then to directly analyze the defect location. The second, more indirect, technique was based on the assumption that the defect contains either  $\alpha$ - or  $\beta$ -stabilizing contaminants of such concentrations that would result in observable local change in  $\beta$  transus temperature. With an appropriate thermomechanical processing such defect can be distinguished from the surrounding by microstructural variation. The details of these techniques and the analyses performed on the rosette defects are as follows.

The 'fish eye' fracture origin of specimen #4 (Figure 5 and 6) was analyzed by Auger electron spectroscopy. One half of the fracture was sectioned longitudinally through the central pore in the 'fish eye' and mounted for metallographic and electron microprobe examination by wavelength dispersive technique. After the Auger and the electron microprobe examinations, the fracture surface and the longitudinal section were studied by secondary ion microprobe technique using an  $32O^+$  primary beam.

In the second technique the approximate location of a rosette-type defect was located in a section of an IMI 685 forging. A compression specimen was then fabricated with the defect located approximately at the center. The specimen was then isothermally compressed at 1830°F to 87% reduction in height using boron

nitride as a lubricant. The compressed specimens was then polished to the expected defect location. The transverse metallographic section was examined optically. The section was then heat treated in vacuum at 1830°F for one hour. The heat treated microstructure was studied optically and by wavelength dispersive electron microprobe techniques.

### III. RESULTS

#### i. LCF Testing of IMI 685 Specimens

##### 1. Defect-Free Material

The room temperature S-N curves of defect-free IMI 685 specimens are shown in Figure 2. Most of these data have been generated by the AF/Metcut. Fatigue behavior is clearly frequency dependent; lower fatigue lives are associated with the lower frequency (12 cph). The frequency effect is especially pronounced at higher stresses. These data will be used as a basis of comparison for specimens failed with rosette-type of fracture.

The differences in fatigue lives at the two frequencies are accompanied by differences in fractographic features. Figure 3 illustrates the appearance of the fracture surface of a specimen which was cycled at the higher frequency (20 cpm). The fatigue region is relatively flat and contains cleavage-like facets on which fatigue striations have been observed. By contrast, the appearance of the fracture at 12 cph is considerably rougher with distinct facets and rather similar to rosette-type of fracture except for the presence of the 'fish eye' in the latter.

##### 2. Defective Material

P&WA has fractured two IMI 685 specimens (#4 and #22) with rosette-type failure. Specimen #4 has a short defect-containing segment diffusion bonded to pull bars. (The fabrication details of this specimen were described in the first Annual Report). Specimen #22 was machined directly from the second piece of IMI 685 forging provided by the AFML. The two specimens differed not only in the fabrication procedures used (e.g. #4 was stress-relieved during diffusion bonding) but also in geometry as the diameters of #4 and #22 are 0.44" and 0.25" respectively. These differences were thought to play a significant role on the fatigue debit of the rosette-type failure(1). In spite of these differences the fatigue lives of these two specimens differ

by only 8% and the fractographic features in both specimens are similar. The fatigue origins were located near the center of both specimens. The only fractographic difference observed was that fatigue striations are observed in #4 but not in #22. This difference will be discussed later.

The LCF lives of all IMI 685 specimens known to have failed with cleavage rosette-type of fracture are shown in Figure 4. As in the case of the defect-free specimens, the fatigue life is frequency dependent. However, it is interesting to observe that specimens failed with rosette-type of fracture have essentially the same lives as the defect-free specimens when tested at 20 cpm. Large fatigue debit associated rosette-type failure is observed only at a frequency of 12 cph.

The scanning electron micrograph of the rosette-type failure (Specimen #4) is shown in Figure 5. The fatigue crack initiated at a macroscopically flat facet about 0.033" diameter which inclines at a small angle to the stress axis. Near the center of this facet is a pore about 0.0002" long. 'River' pattern are observed to originate from this pore. Further, 'brittle-type' striations have been observed on the facet, the formation of this type of striation will be discussed later. Details of the 'fish eye' crack nucleation site are illustrated in Figure 6. The topography surrounding the 'fish eye' is highly irregular and consists of cleavage-like facets. Fatigue striations have been observed only on facets A, B, and C (Figure 7). The measured striation spacings on these facets will be discussed later with reference to crack growth data. Either cleavage-like or overload type of cracking occurred between these facets. The dimensions of all the facets are about the same as those of the acicular alpha colony packets in this material.

### 3. Seeded (Defective) Material

The LCF results of seeded IMI 685 specimens relative to those of the defect-free and rosette-containing specimens are illustrated in Figure 8. The data points from specimens seeded with hydride are indicated by H, while those seeded with clean pores are indicated by P. The frequency effect on fatigue life is again obvious. Specimens tested at the lower frequency of 12 cph (filled circles) have fatigue lives about one order of magnitude lower than those tested at the higher frequency of 20 cpm (pen circles). Relative to the 20 cpm LCF lives of defect-free and rosette-

containing specimens, the seeded specimens show a life reduction of one order of magnitude even though the size of the seeded pore is equivalent to that of the 'fish eye' fatigue origin. This observation together with the appearance of the fracture surfaces described below indicate that the integrity of the diffusion bond is questionable. Even so, the large fatigue debit of a rosette-type failure at 12 cph has not been reproduced exactly in the hydride-seeded specimens.

Fractographic analysis shows that fracture initiated at the seeded defects in all the specimens tested. The fatigue fracture areas show features similar to those described in the two previous sections. However, the surrounding tensile fracture followed the diffusion bond interface even though the separation was by ductile tearing. This observation may indicate inadequate bonding. The effects of the diffusion bond on the observed fatigue lives are not necessarily very large since it has been observed that the fatigue life of a specimen (DB #32) in which the tensile fracture path did not involve the diffusion bond, was about 17% higher than the ones which separated along the bond interface.

## ii. Chemistry Determination on Rosette Defects

### 1. IMI 685 Specimen #4

#### Secondary Ion Microprobe Results

Determination of local chemistry on the fracture surface was found to be rather difficult even though the fracture origin (fish eye) is relatively flat. The low sputtered ion yield prevented meaningful ion image being obtained. In addition, the non-reflectivity and varying focal depth also prevented exact correlation with scanning electron micrographs of the regions from which the secondary ions were generated. Consequently, data was obtained from the longitudinal section of the fracture only. These data were recorded after the contaminated surface layer was sputtered away. The relative changes in concentrations of several elements during sputtering is shown in Figure 9 which was obtained near the fracture origin. The relatively high initial concentrations of Na, Si and C are due to surface contamination. These decreased as steady

stable levels of major constituents Ti and Al were approached. Current data taken after sputtering for one to two hours were reduced to the concentrations listed in Table I. These results may be compared meaningfully on a relative basis, but have known errors on an absolute sense. For instance, it has been established in previous studies that the data reduction scheme used produces high results for aluminum. On a relative basis, Table I indicates that the most significant difference between the fracture origin and the bulk is in the N contents, it is slightly over four times higher at the origin. Contrary to popular speculation, the H content at the origin was found to be lower than that in the bulk by a factor of two. Other differences are small but tend to indicate that the fracture origin is lower in  $\alpha$ -stabilizing elements Al and C and higher in  $\beta$ -stabilizing elements Fe and B.

#### Optical Metallography, Auger Spectroscopy and Electron Microprobe Analysis

Optical metallography revealed no microstructural anomaly at the 'fish eye'. The electron microprobe results showed no detectable difference in chemistry at the fracture origin. However, the sensitivity of the electron microprobe technique for detecting interstitials is known to be poor, especially at low concentrations. Some of the results of the Auger electron spectroscopy (AES) are shown in Figure 10 which were obtained at the fracture origin before (Figure 10a) and after sputtering (Figure 10b). It can be seen that the sputtering reduced the concentrations of S, C and O which are common surface contaminants. The nitrogen peak coincides with one of the Ti peaks and therefore its concentration cannot be readily determined. No significant difference was observed between the AES results at the fracture origin and bulk material.

#### 2. Thermomechanically Processed Specimen

The microstructure of the rosette defect-containing specimen after isothermally compressed at 1830°F to 87% reduction in height is shown in Figure 11. Recrystallization has occurred heterogeneously throughout the sample, and revealing no clear-cut microstructural difference at the expected defect site. Additional recrystallization occurred when the compressed specimen was heat treated at 1830°F for one hour. However, many localized areas remained unrecrystallized. The microstructure after the heat treatment is

reminiscent of the presence of  $\beta$ -fleck defects. The results of the electron microprobe analyses of the recrystallized and unrecrystallized regions (Figure 12) are shown in Table II. The data represents relative compositions averaged over an area of  $10^{-4}$  cm<sup>2</sup>. Although the differences between the recrystallized and unrecrystallized regions are small, a definite trend can be detected. The unrecrystallized region shows higher concentrations of the  $\beta$ -stabilizing element Mo and lower concentrations of the  $\alpha$ -stabilizing elements Al and Zr than the recrystallized region.

### iii. LCF Testing of Seeded Specimens from Other $\alpha$ - $\beta$ Ti Alloys

The LCF lives of the Ti-6Al-4V specimens seeded with various contaminants are given in Table III. Among the contaminants used Al, TiN, NaCl and hydride, only TiN and NaCl appear to have an effect on fatigue life. Degradation of fatigue life by a factor of about three is observed for these contaminants. However, it should be emphasized that the hydride used for this group of specimens has a hydrogen content of 0.35% while those used previously have a hydrogen content of 1.2%. This may have affected the present results.

The scanning electron fractography showed that the fatigue fracture was initiated at the seeded defects in all specimens with possibly one exception, DB #24 in which the seeded defect could not be located. None of the specimens fractured along the diffusion bond. Further, the locations of the seeded defects varied in these specimens, some being located in the center while others were near the edge. As will be discussed later the location of the seeded defect has an effect on fatigue life which is rather small compared with the usual scattering in LCF data. The fractographic features in all these specimens show very little difference. A typical scanning electron fractograph of a subsurface initiated and propagated fatigue crack is shown in Figure 13a, that of a near-surface initiated fracture is shown in Figure 13b. Both of these specimens were seeded with hydride and have equivalent fatigue lives. In Figure 13a the fatigue origin (hardness indentation) which is partially exposed can be located at the center of the micrograph. Figure 13a shows that the topography of the fatigue propagated region appears to be rougher than that of the surface or near surface initiated fracture. Striations could be found only on facet A, and are illustrated in Figure 14a. These striations bear little resemblance to ductile-type fatigue striations. The appearance of the striations observed on facet B of the near-surface initiated fracture shown in Figure 13b

PRATT &amp; WHITNEY AIRCRAFT

is illustrated in Figure 14b. The appearance of the fracture shown in Figure 13a and b are similar to those of the IMI 685 (Figures 5 and 3 respectively) except in the scale of the fracture surface topography, being relatively finer in the seeded Ti-6Al-4V specimens. This difference can be directly related to the scale of the microstructures, specifically the beta grain size and colony dimensions, in these materials.

The LCF lives of Ti-6Al-2Sn-4Zr-2Mo seeded with argon pores are shown in Table IV which also indicates the diffusion bond conditions used. The fractographic features of the first specimen tested (#29) consist of a central region where the argon is located and a peripheral region both of which show evidence of good bonding. Between these two regions is an area on which the markings on the original surface are clearly visible. The formation of this apparently unbonded region was due to incomplete removal of argon during diffusion bonding. The difficulty was largely eliminated in the third specimen (#40) when argon was evacuated at about 200°F. However, small regions of unbonded areas were evident on the fracture surfaces, indicating the inherent difficulty of completely removing argon, once introduced. Conversely, the absence of unbonded areas on fracture surfaces of IMI 685 failed with rosette-type fracture suggests that no argon contamination was involved in the fracture. Ironically, the specimen that appears to have the best diffusion bond (#40) has the shortest fatigue life.

#### IV. DISCUSSION

There are two important aspects in the rosette-type fracture, the characteristic fractographic features and the large fatigue debit, both of which must be taken into consideration in order to provide a basic understanding of this phenomenon. The following is one such attempt which, unlike previous ones, has the advantage of a larger data base.

##### i. Fractographic Features

A common and distinctive fractographic feature of rosette-type failure is the formation of the 'fish eye' fracture origin. The characteristics of the 'fish eye' are its dimension (0.005"-0.040"), the presence of pores (.0001"-.0008") and brittle-type striations (Figure 6). The pores has been traced to the casting porosity which failed to heal during forging<sup>(1)</sup>. It should be remembered however that in the early part of this study testing of specimen #2 exhibited a very low life but no clear cut 'fish eye' at the subsurface origins. (This specimen was cut in the

radial forging direction rather than the transverse orientation of specimens #4 and #22). Brittle striations were observed in specimen #2 adjacent to the fracture origin which may indicate that the failure mechanism was the same. However, a well defined 'fish eye' seems typical of the transverse direction implying perhaps that the conditions for formation derive from billet breakdown rather than the final forging operation. The flat region in the 'fish eye' has been attributed to the cleavage of an alpha colony packet since they are dimensionally consistent<sup>(3)</sup>. The presence of the brittle-type striation has not been satisfactorily explained. A mechanism which will lead to the formation of the striation is now proposed. It is depicted schematically in Figure 15a. Heterogeneous plastic deformation in coarse acicular microstructure would result in intense slip bands and formation of microcracks at the slip offsets in the acicular  $\alpha$  phase (Figure 15b, side view of Figure 15a). When the shear plane is not microscopically flat, irregularly spaced markings parallel to the direction of shear will be left on the shear plane (Figure 15c, top view of Figure 15a). The connection between the pore and the 'fish eye' is not obvious since it is too small to have an appreciable effect in LCF crack initiation. However, as shown in the secondary ion microprobe results that the pore region may be contaminated with nitrogen and resulted in local embrittlement. The test results on specimen #2 may imply the contamination is spherically symmetric.

The highly irregular fracture surrounding the 'fish eye' is a consequence of the microstructure of the material and the test conditions used. Two different modes of fatigue crack propagation have been observed in IMI 685 which has an acicular microstructure with large  $\alpha$  packet and prior beta grain sizes. The fatigue crack propagates predominantly along a plane of maximum tensile stress when cycled without a dwell, i.e., the direction of fatigue crack propagation is only stress dependent. When a dwell at maximum load is imposed, the fatigue crack propagates preferentially along a path normal to the longitudinal axis of the acicular  $\alpha$  phase<sup>(4)</sup>.

The corresponding difference is reflected in the appearance of the fracture. The fatigue propagated region of the specimen tested at 20 cpm is relatively flat (Figure 3). On the other hand, when a dwell is imposed the fatigue region is highly irregular since the crack front changes direction upon entering a differently oriented  $\alpha$  colony. The degree of irregularity of the fracture surface depends directly on the scale of the microstructure.

PRATT &amp; WHITNEY AIRCRAFT

The presence of fatigue striation in IMI 685 #4 which failed with a subsurface origin (Figure 5) is an exception to our experience with Ti-6Al-4V. With either an equiaxed or acicular microstructure, fatigue striations are conspicuously absent in the seeded Ti-6Al-4V specimens until the cracks reached the surface. The absence of the ductile-type fatigue striation was thought to be attributable to the better reversibility of the slip during fatigue deformation in an ultimate vacuum created in a subsurface opening. However, as Bowen has demonstrated recently that the symmetry of the active deformation modes relative to the crack plane must also be taken into consideration in determining the nature of the striations and the ease with which they can be observed<sup>(5)</sup>. For instance, striations were readily observed when the fracture system (i.e. fracture plane and direction) was  $\{10\bar{1}0\} \langle \bar{1}2\bar{1}0 \rangle$ , whereas when the fracture system was  $\{0001\} \langle \bar{1}2\bar{1}0 \rangle$  striations were difficult to observe. The unusual occurrence of striation in specimen #4 may be associated with some particular orientations of the facets on the fracture plane which strongly favors the formation of striations.

ii. The Fatigue Debits in IMI 685

The large fatigue debit of IMI 685 associated with the subsurface rosette-type fracture have been investigated independently by several laboratories in the past. The 'rosette debit' has been rationalized in terms of the initial presence of the 'fish eye' fatigue origin and the enhanced fatigue crack propagation rate possibly due to the R and dwell effect<sup>(1)</sup>. However, the magnitude of the 'rosette debit' has not been defined or analyzed in any detail in these terms and therefore the origin of the debit remained a mystery. In the following we shall discuss in detail the 'rosette debit' in light of the results from previous investigators as well as those generated in this investigation.

Prior to a discussion of the 'rosette debit' it is interesting to examine the cause of the shorter fatigue life of the defect-free specimens, especially at higher stresses, when tested with a dwell. This 'dwell debit' and the 'rosette debit' are defined schematically in Figure 16. As will be explained these two debits are related only superficially. Rolls Royce<sup>(1)</sup> measured significantly faster crack propagation rates when dwell cycles were used (12 cph) than those measured at a faster frequency (10 Hz), thus the Rolls Royce's explanation for the 'dwell debit' which was also assumed to be a component of the 'rosette debit'. On the other hand, AF/Metcut data revealed no effect

PRATT &amp; WHITNEY AIRCRAFT

of frequency on fatigue crack propagation rate\*. Their results are shown in Figure 17. According to the AF/Metcut data the 'dwell debit' may be explainable in terms of the possible difference in crack nucleation life which is assumed to be much shorter when tested with a dwell than that without a dwell. This difference has not been demonstrated, however.

From above discussion for the 'dwell debit' it appears possible to account for the 'rosette debit' by the initial presence of the 'fish eye' fracture origin which forms in a very small number of cycles and the higher propagation rate measured by Rolls Royce (Curve A Figure 15). The fatigue lives calculated using the central penny-shaped crack model<sup>(6)</sup> are shown in Figure 18. The calculations were made using initial crack radii of 0.01" and 0.02" and using either the crack propagation behavior measured by the AF/Metcut (band C) or that measured by Rolls Royce (band A). It can be seen from Figure 1<sup>9</sup> that the calculated lives are in reasonable agreement with those observed only in the case when the specimens were tested without a dwell (data points indicated by open circles). With a dwell, the observed lives are lower than those calculated by about two orders of magnitude even using the fastest crack propagation rates measured (band A). It may be argued that these calculations are valid only in the tests without an imposed dwell which result in a rather planar fatigue propagation (Figure 2). Applicability is limited in cases where a dwell is imposed, since crack propagation is microstructure sensitive and a highly irregular crack path is observed. This anisotropy of crack propagation is thought to play an important role in the 'rosette debit' since the dimension of the 'fish eye' fracture origin is about the same as the  $\alpha$  packet size. It should however be pointed out that anisotropy effect works in both directions, i.e., it can either enhance the rate of crack propagation or can slow it down. One should therefore observe a very large scattering in the fatigue lives of the dwell-tested specimens. Clear trends in fatigue lives of dwell-tested defect-free specimens and rosette-containing specimens would not be possible if the anisotropy effect were overwhelming. This is contrary to observation. Therefore the large discrepancy between the calculations and the 'rosette lives' is taken to suggest that the 'rosette debit' cannot be explained simply from the initial presence of the

\*Subsequent measurements by Rolls Royce on IMI 685 which had been given a faster cooling than that used previously showed no frequency effect on crack propagation rate<sup>(1)</sup>.

'fish eye' fracture origin and the dwell effects on crack propagation. Evidence supporting this contention is cited below.

The ion microprobe results indicate that the 'rosette debit' is associated with a significantly higher concentration of nitrogen around the 'fish eye' fatigue origin (Table I). The enhanced crack propagation rates have also been measured on facets A, B and C (Figures 5 and 7) which are shown in Curve D of Figure 19. The striation measurements show that the crack propagated initially at significantly higher rates than those measured but tend to decrease toward the measured values at large  $\Delta K$  i.e. away from the 'fish eye' origin. Using the crack propagation behavior described by Curve D and A, the calculated fatigue life is about 1000 cycles. The actual fatigue life of this specimen is 1600 cycles. This small discrepancy indicates that the analysis used is reasonably self-consistent.

A preliminary conclusion from these observations is that the large 'rosette debit' observed in IMI 685 is attributed primarily to the nitrogen contamination which results in amplification of local crack growth rates. As the calculations show the initial presence of the 'fish eye' fatigue origin which by itself in no fatigue debit except possibly at low stresses, is of secondary importance in accounting for the 'rosette debit'. It should be reiterated that the origin of the 'rosette debit' is distinctly different from the 'dwell debit' although the conditions leading to their manifestation are seemingly the same. The 'dwell debit' occurs in defect-free material. It is associated with shorter initiation life<sup>(2)</sup> and/or faster crack propagation rates<sup>(1)</sup> but no nitrogen contamination is involved. Obviously work in the final section of this work will center on defining in more detail the influence of nitrogen on the LCF properties of IMI 685 with an acicular microstructure.

### iii. Seeded specimens of Other $\alpha$ - $\beta$ Ti Alloys

Several aspects in the LCF results of the seeded specimens contribute toward an understanding of the effects of subsurface defect on LCF properties in general and cleavage rosette-type of fracture in particular. For instance, the results of specimens seeded with argon indicate that material contaminated with argon is likely to show the telltale sign of unbonded areas. The similarity of the fractographic features between  $\beta$  heat treated Ti-6Al-4V and IMI 685 shows that the only unique feature in the rosette fracture is the presence of the 'fish eye' fatigue origin which can be duplicated, perhaps, by embedding contaminant in a smaller indentation (.003"). Although fatigue

PRATT &amp; WHITNEY AIRCRAFT

debits have been observed in TiN-seeded Ti-6Al-4V specimens with either equiaxed microstructure or acicular microstructure, the magnitude of these debits are relatively small. However, the seeded Ti-6Al-4V specimens had been tested only at 1 cpm. A slower frequency (12 cph) may increase the debit significantly as is the case in IMI 685. The LCF results of the seeded Ti-6Al-4V specimen also show that for a given type of seeded flaw, the LCF lives are relatively insensitive to the exact location of the flaw in the gage area. Indeed, fracture mechanic calculations of two extreme cases, surface-initiated fracture and center-initiated fracture, show a relatively small difference of about 20% in fatigue life which is smaller than the usual scattering in LCF data.

REFERENCES

1. Rolls Royce presentation at the AFML Seminar on Defects in Titanium Alloys, Wright-Patterson Air Force Base, Ohio, 1973.
2. Metcut Report No. 1069-19640-2, February 1975, Cincinnati, Ohio.
3. D. Eylon, Private Communication, 1976.
4. R.H. Jeal, Paper No. 28.6 TMS-AIME Fall Meeting, September 1976, Niagara Falls, New York.
5. A.W. Bowen, Acta Met., 23, pp. 1401-1409 (1975).
6. F. Erdogan and G.C. Sih, J. Bas. Engng., 85, 519 (1963).

TABLE IION MICROPROBE ANALYSES OF  
ROSETTE FRACTURE IN IMI 685

<u>Element</u>	<u>In Bulk</u> (Atomic Percent)	<u>Near Origin</u>
Li	$3.6 \times 10^{-4}$	$3.0 \times 10^{-4}$
B	$1.46 \times 10^{-2}$	$2.55 \times 10^{-2}$
C	0.89	0.54
Al	30.91	23.49
Si	1.51	1.55
Fe	0.23	0.28

(Relative Ion Intensities Ti = 1.0)

H	$2.5 \times 10^{-4}$	$1.1 \times 10^{-4}$
N	$2.7 \times 10^{-6}$	$11.2 \times 10^{-6}$
Cl	$7.7 \times 10^{-6}$	$10.7 \times 10^{-6}$

TABLE II

## ELECTRON MICROPROBE ANALYSES OF FORGED IMI 685

<u>Element</u>	<u>No. of Counts in 100 Sec.</u>	
	<u>Equiaxed Microstructure*</u>	<u>Acicular Microstructure*</u>
Al	39920	36470
Zr	2420	2410
Mo	693	721

\*See Figure 12

TABLE III

## LCF LIVES OF SEEDED Ti-6Al-4V SPECIMENS

C-110 KSI, 1 cpm)

<u>Seeded Defects</u>	<u>No. of Cycles to Failure (Specimen No.)</u>
None, Control Specimen	26,230 (J-11)
Pore (0.02" Diagonal)	5,870 (#26)
Pore Containing Al	6,360 (#23)
Pore Containing TiN	2,430 (#22)
Pore Containing NaCl	2,460 (#24) 2,690 (#25)
Pore Containing Ti-6Al-4V Hydride	6,660 (#21) 6,660 (#27) 14,260 (#28)

TABLE IVLCF LIVES OF Ti-6Al-2Sn-4Zr-2Mo  
SEEDED WITH ARGON

<u>Diffusion Bond Conditions</u>	<u>No. of Cycles to Failure (Specimen No.)</u>
1750°F/500 psi/4 hr. Ar Evacuated at 800°F	730 (#29)
1850°F/560 psi/4 hr. Ar Evacuated at 800°F	812 (#30)
1850°F/560 psi/4 hr. Ar Evacuated at 200°F	57 (#40)

FIGURE CAPTIONS

1. Experimental setup for seeding an argon pore in two rods which were subsequently diffusion bonded together and machined into a LCF specimen.
2. S-N curves of defect-free IMI 685 specimens tested at either  $R = 0-0.3$ , 20 cpm or  $R = 0.3$ , 12 cph.
3. Scanning electron fractograph of IMI 685 specimen #6 which was fractured at 0-110 KSI, 20 cpm. Note the relatively flat fatigue-propagated area around the crack origin at A.
4. S-N curves of IMI 685 specimens which failed with rosette-type fracture.
5. Scanning electron fractograph of a rosette-fracture observed on IMI 685 specimen #4. Details of the 'fish eye' fracture origin are shown in Figure 6. Striations have been observed on facets A, B and C. Those on facet A are shown in Figure 7.
6. (a) The topography of the 'fish eye' crack nucleation site.  
(b) Detailed appearance of the central pore and its surrounding. Note the presence of the brittle-type striations on the 'fish eye'.
7. (a) Replica showing fine fatigue striations between facet A and the 'fish eye' on the fracture surface illustrated in Figure 6.  
(b) JEM showing fatigue striations on facet A.
8. The LCF lives of seeded IMI 685 specimens relative to those with and without rosette defects. The data points from specimens seeded with Ti-6Al-4V hydride are indicated by H and those from specimens seeded with clean pores, by P. The open circles indicate tests without dwell (i.e. at 20 cpm) and the filled circles indicate tests with dwell (i.e. at 12 cph).
9. Change in intensities of several elements as a function of sputtering time. Determination of compositions at the 'fish eye' fracture origin and the bulk commenced after steady levels of major elements were observed.

10. Auger electron spectrographs at the 'fish eye' fatigue origin.
  - (a) before sputtering
  - (b) after sputtering, note the decrease in C, O and S which are common surface contaminants.
11. Microstructure near the expected rosette defect site in an IMI 685 specimen which had been isothermally compressed at 1830°F.
12. The microstructure shown in Figure 11 after additional recrystallization anneal at 1830°F for 1 hour.
13. Scanning electron fractographs of hydride seeded Ti-6Al-4V specimens with acicular microstructure.
  - (a) center-initiated fracture (DB#27)
  - (b) near-surface-initiated fracture (DB#21)
14. (a) Striations observed on facet A of the fracture surface shown in Figure 13(a).
  - (b) Striations observed on facet B of the fracture surface shown in Figure 13(b).
15. Mechanism of brittle-striation formation on the 'fish eye' of the rosette-fracture in IMI 685 alloy.
16. Schematic diagram showing the 'dwell debit' and the 'rosette debit' in IMI 685 alloy.
17. Crack propagation data on IMI 685 alloy.
18. Comparison of the calculated fatigue lives with those of IMI 685 specimens which failed with rosette-type fracture with a dwell (filled circles) without a dwell (open circles). The calculations were made using penny-shaped crack radii of 0.01" and 0.02" with either the Rolls Royce crack propagation data (band A) or the AF/Metcut data (band C).
19. Striation spacings measured from IMI 685 specimen #4 (Figures 5 and 7) plotted as a function of  $\Delta K$  which are calculated using the central penny-shaped crack model<sup>6</sup>.

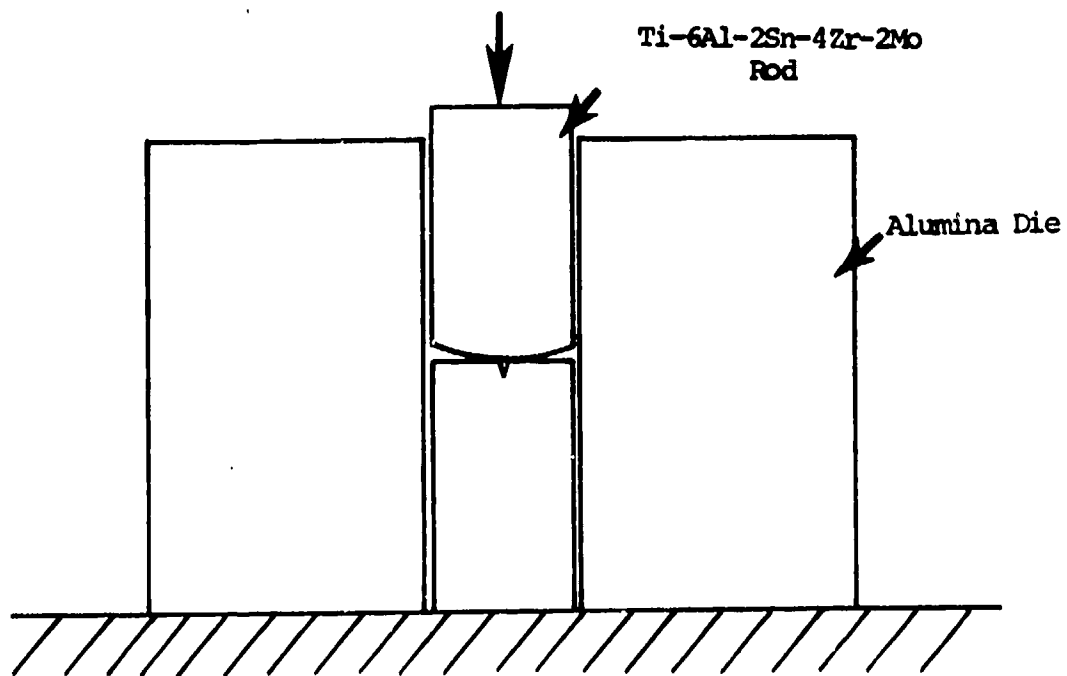


Figure 1

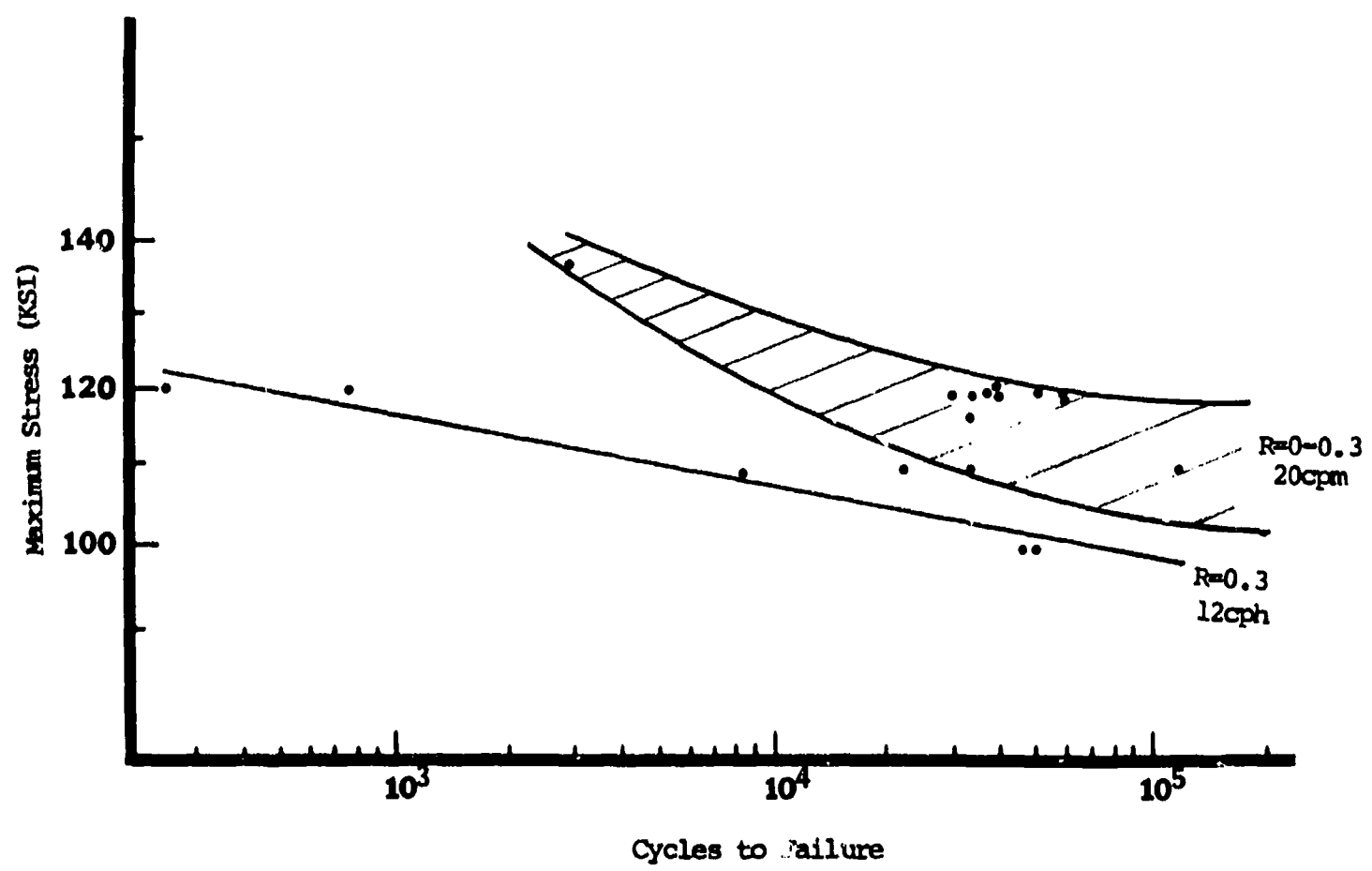
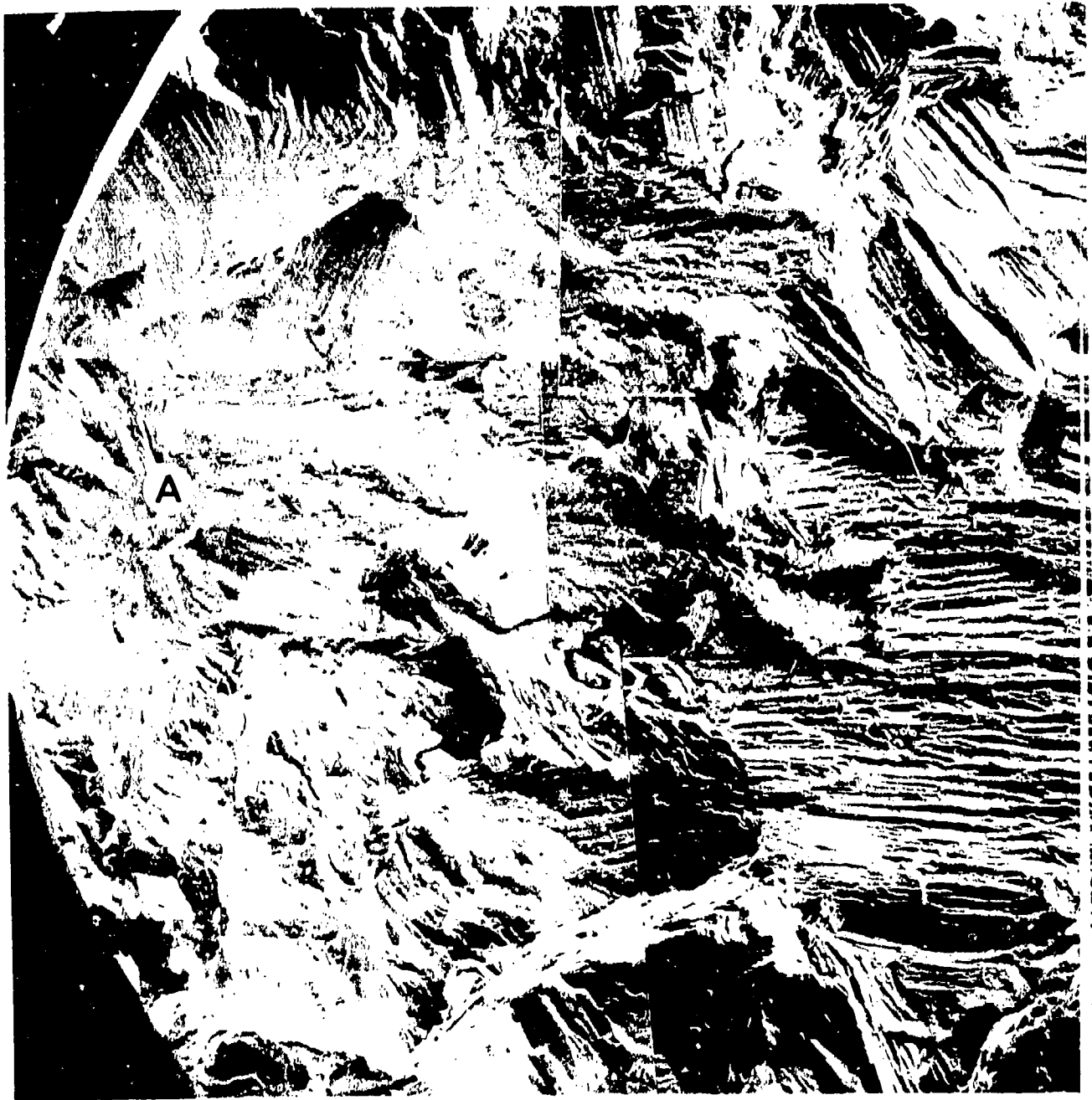


Figure 2



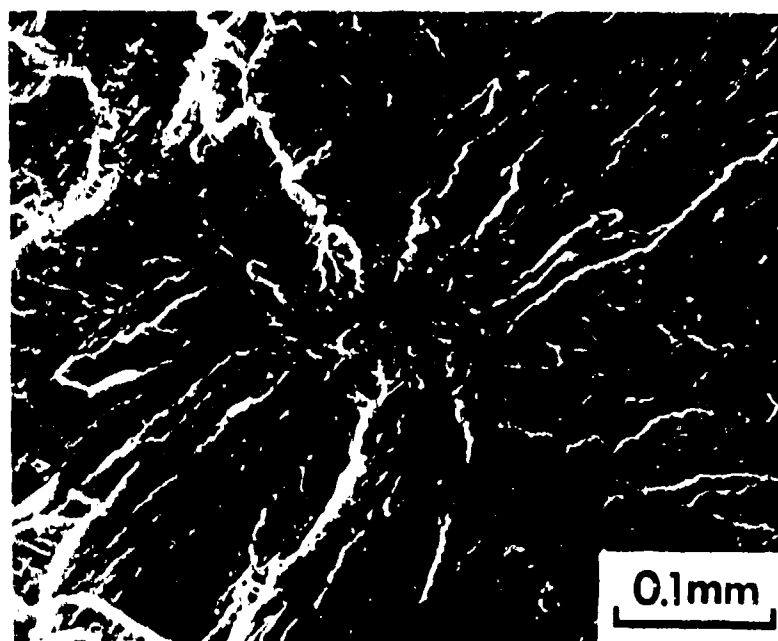
0.5 mm

Figure 3

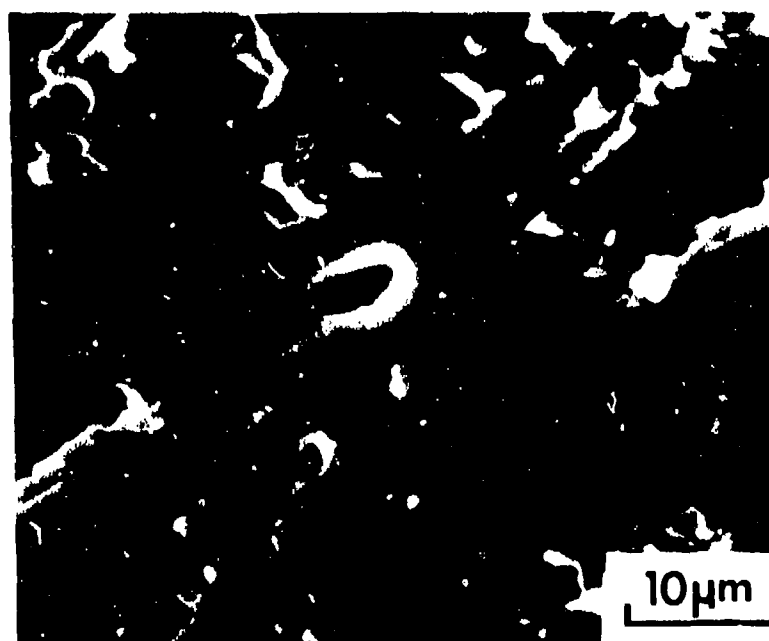




Figure 5



a



b

K-20902

Figure 6



10 $\mu$ m



20 $\mu$ m

Figure 7

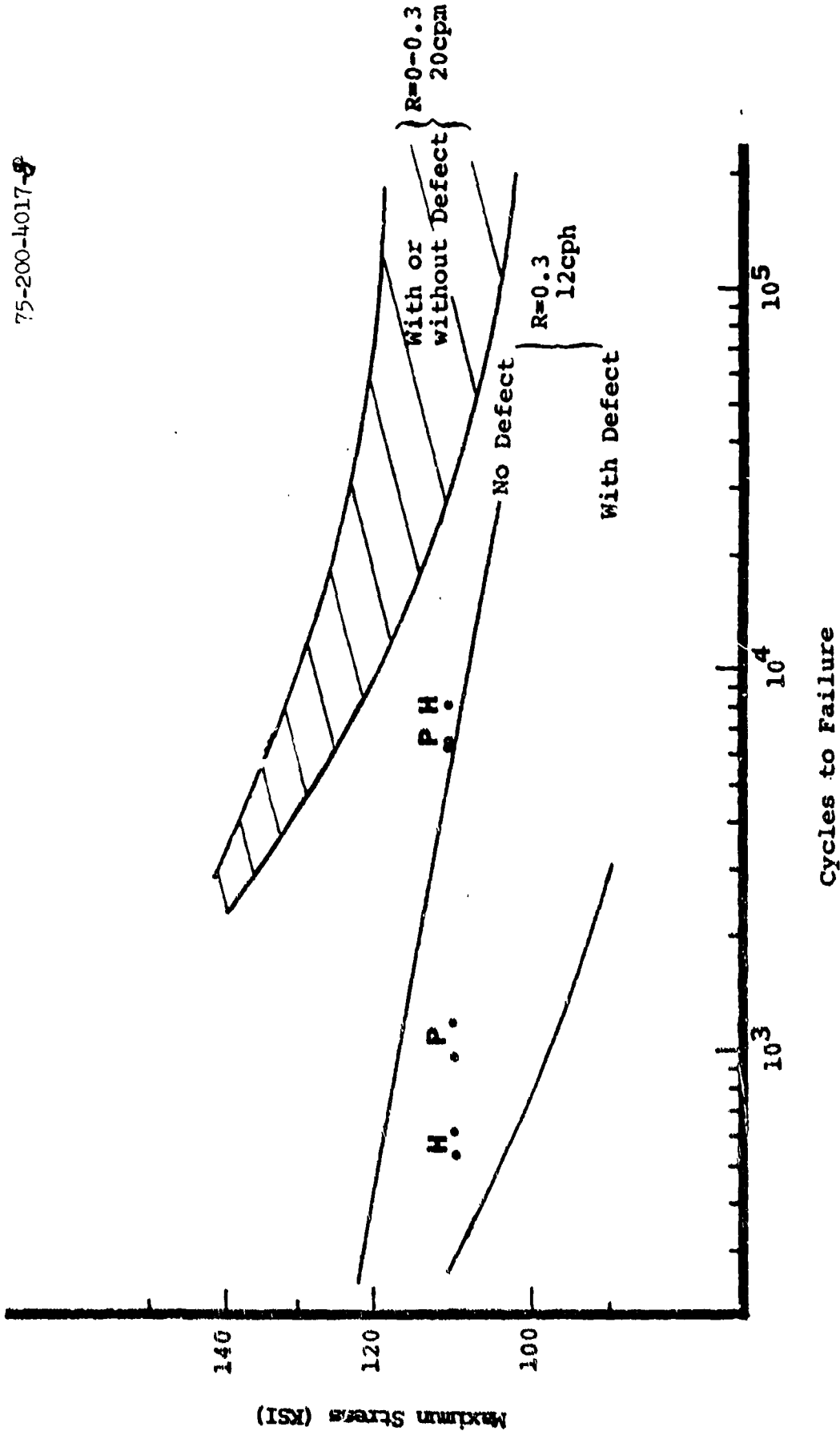


Figure 8

## IMI-4 CROSS-SECTION (ORIGIN)

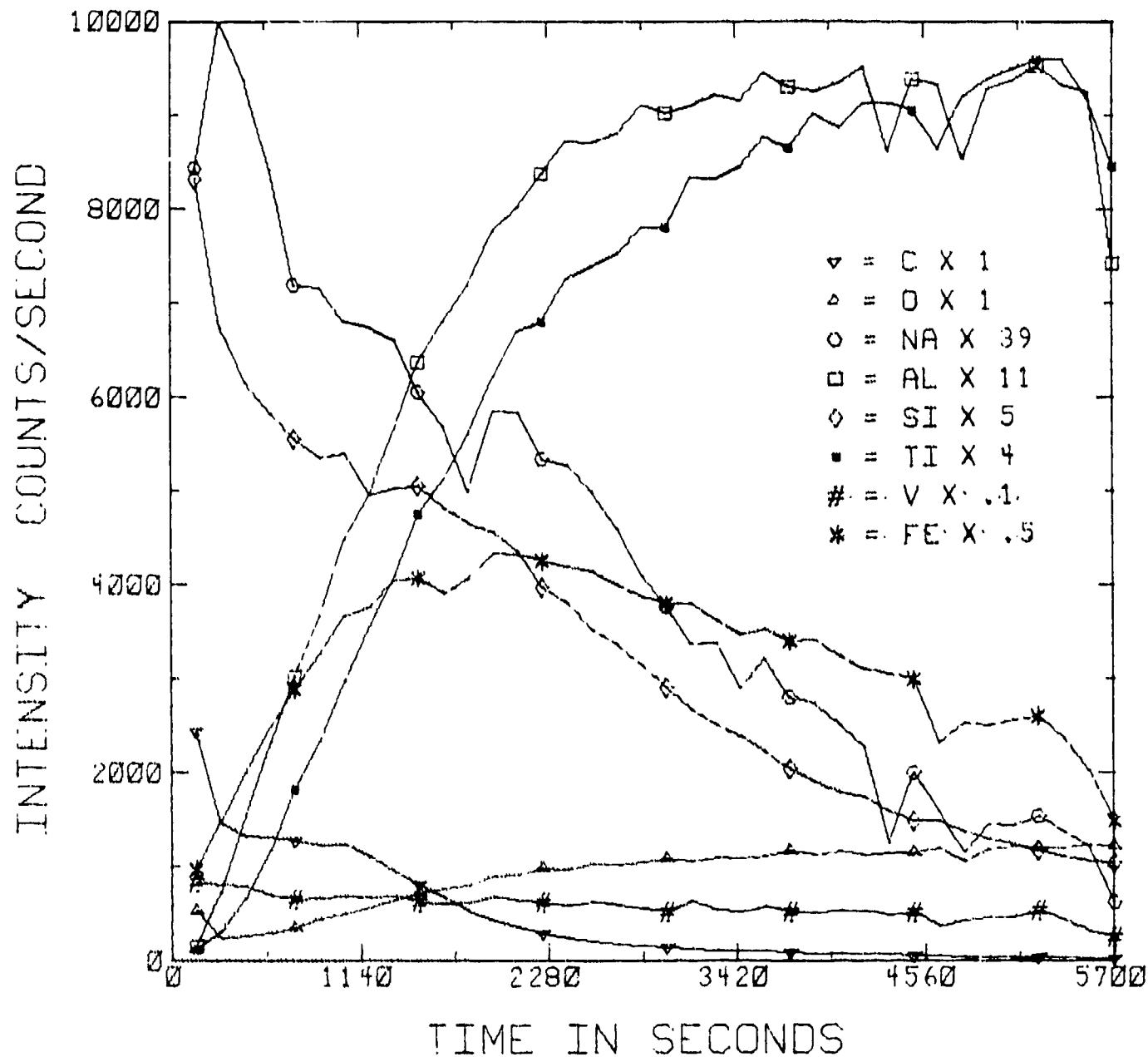


Figure 9

75-200-4017-5

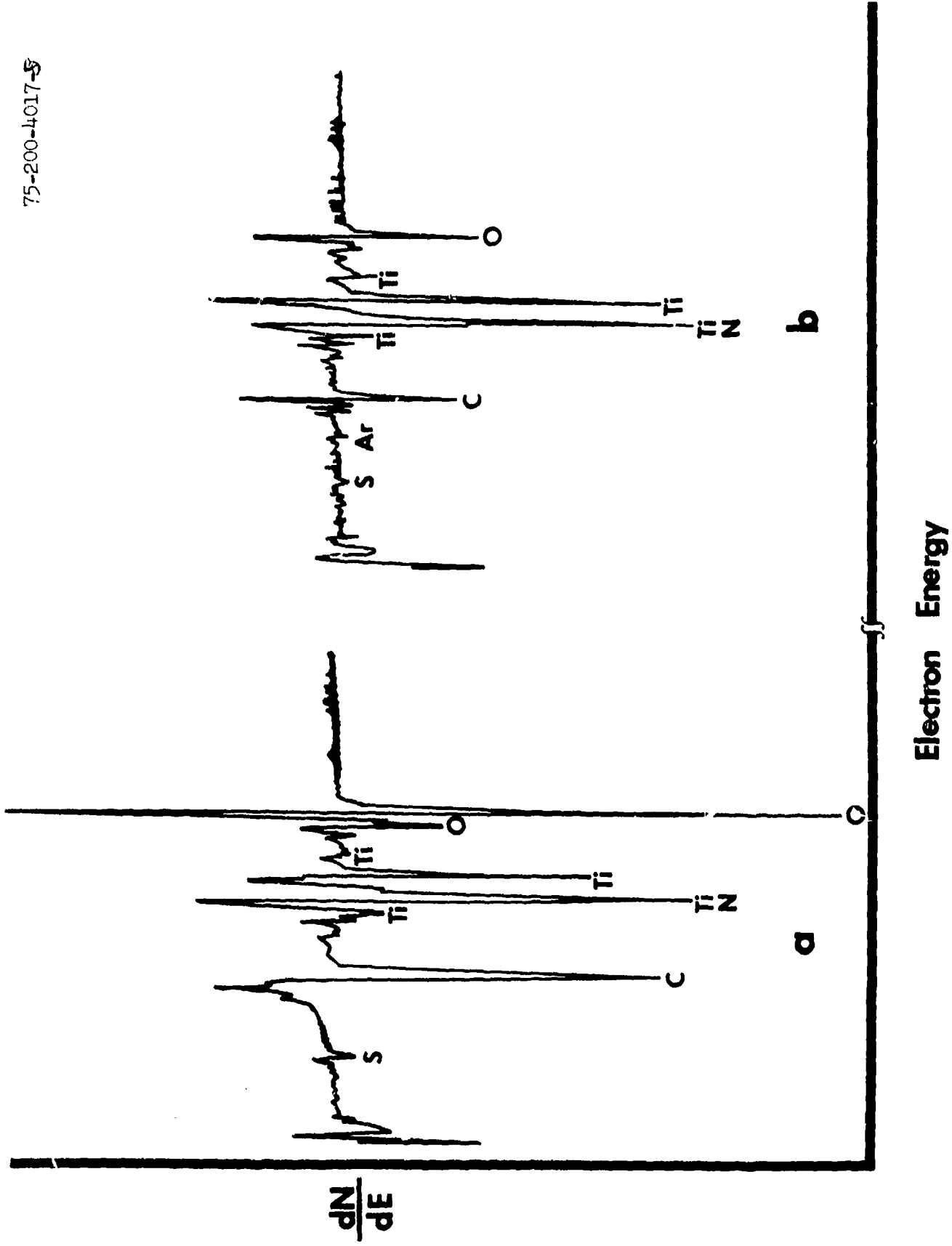


Figure 10

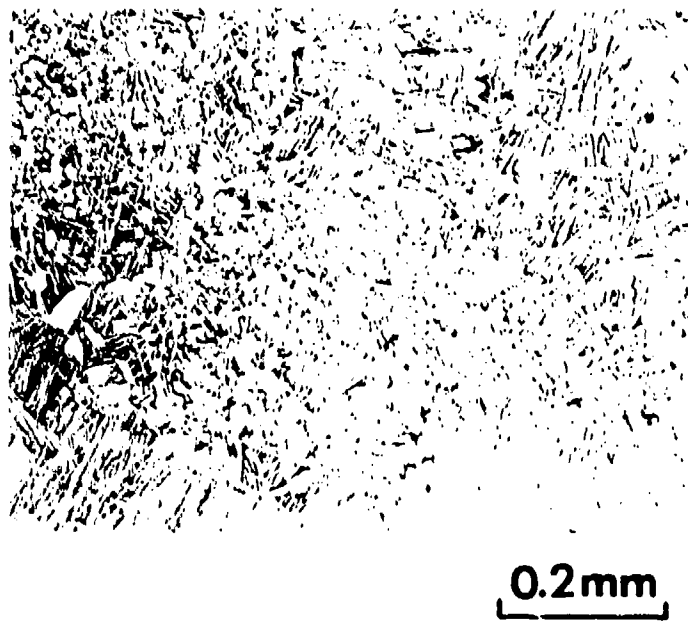
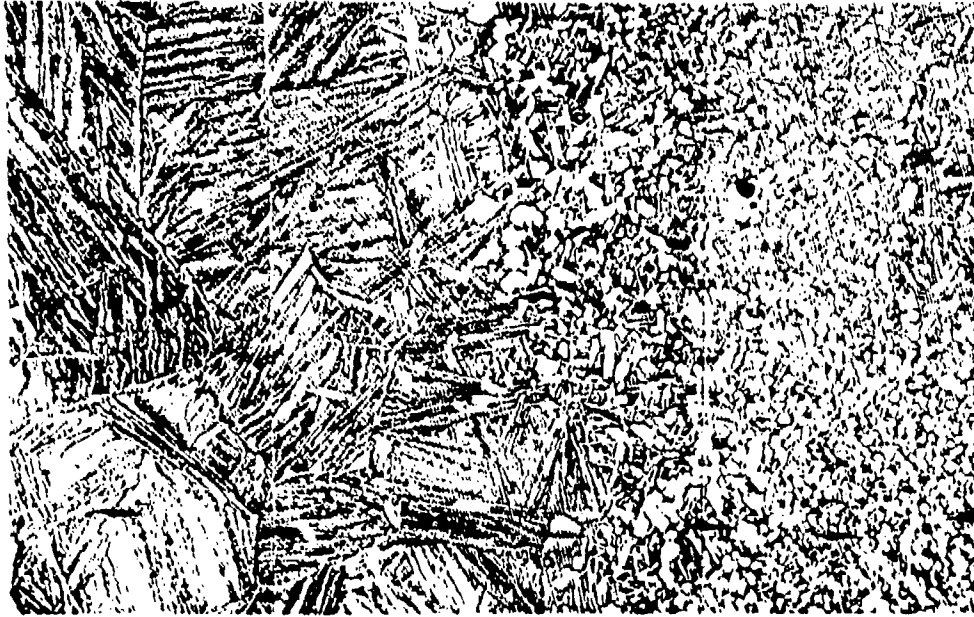


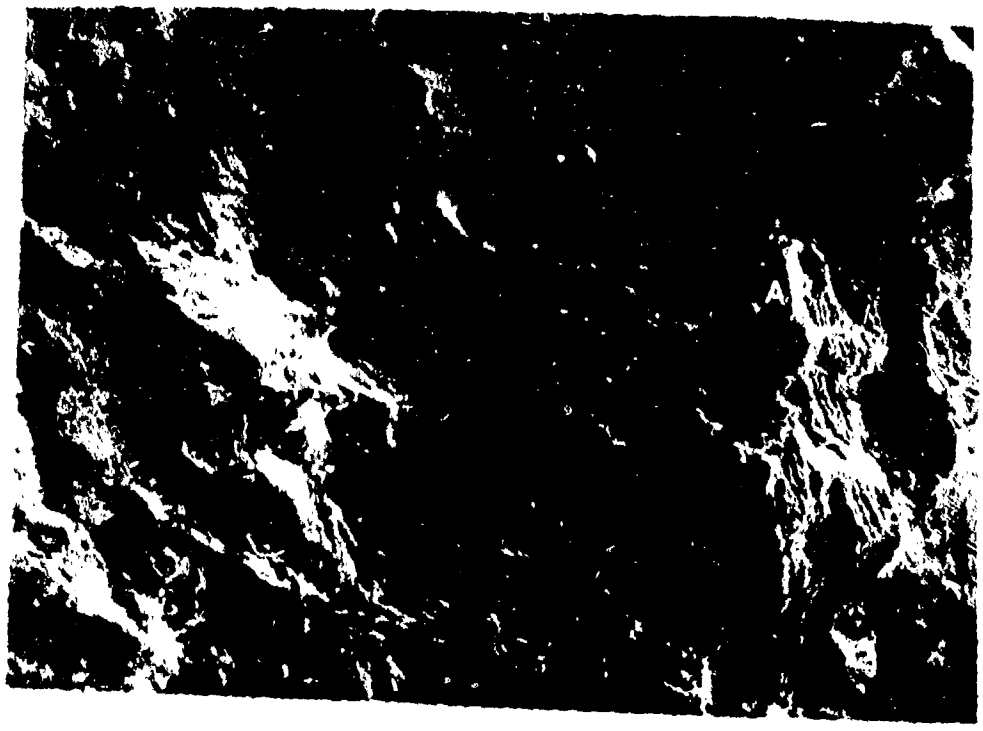
Figure 11



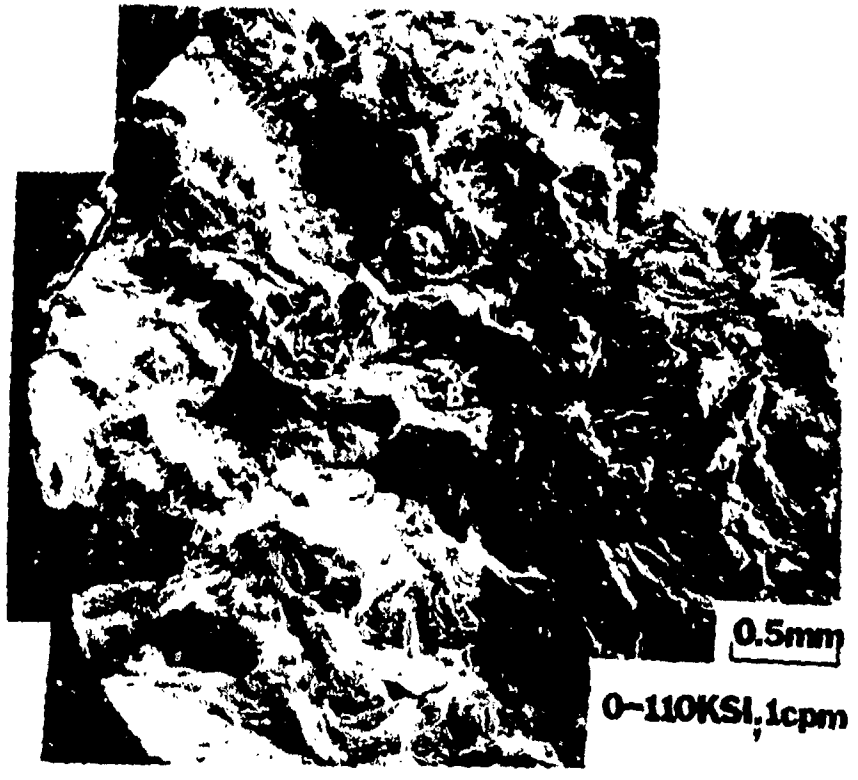
0.2mm

Figure 12

**Ti-6Al-4V Hydride Pore**

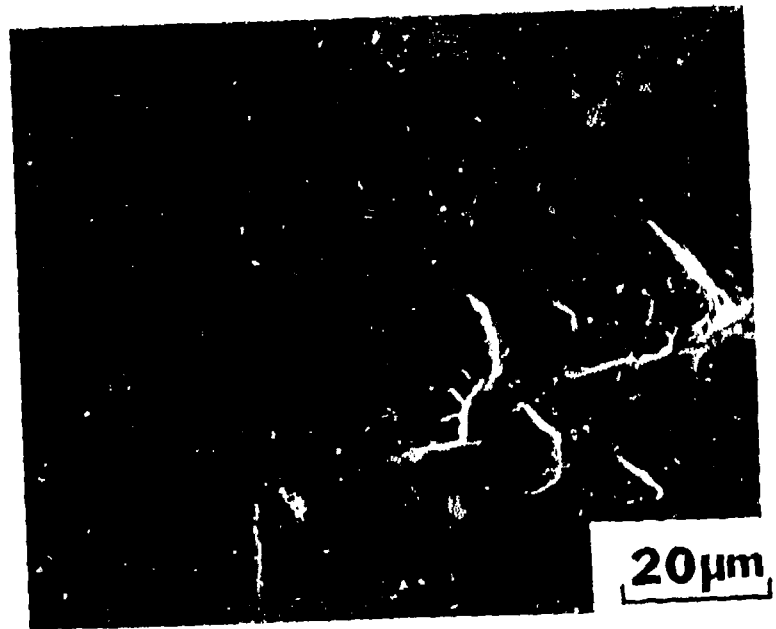


**N<sub>F</sub> = 6655**

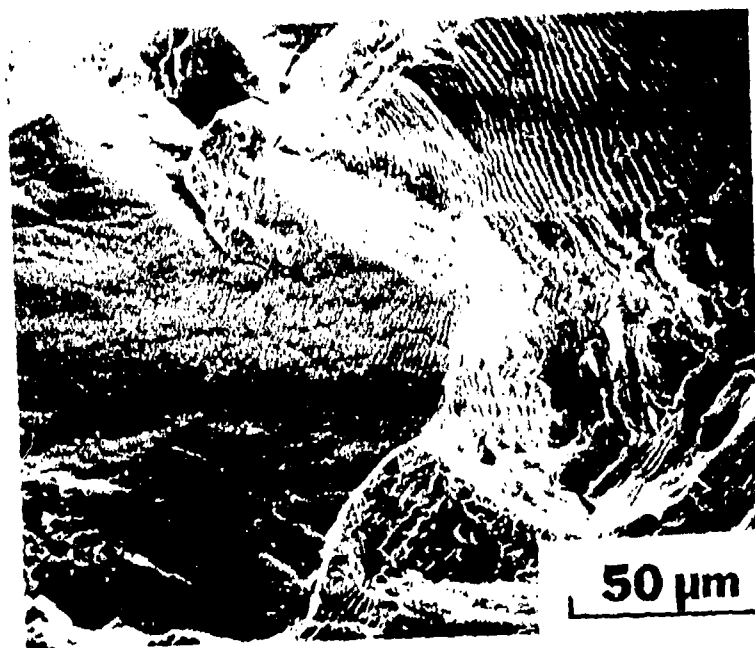


**N<sub>F</sub> = 6656**

Figure 13

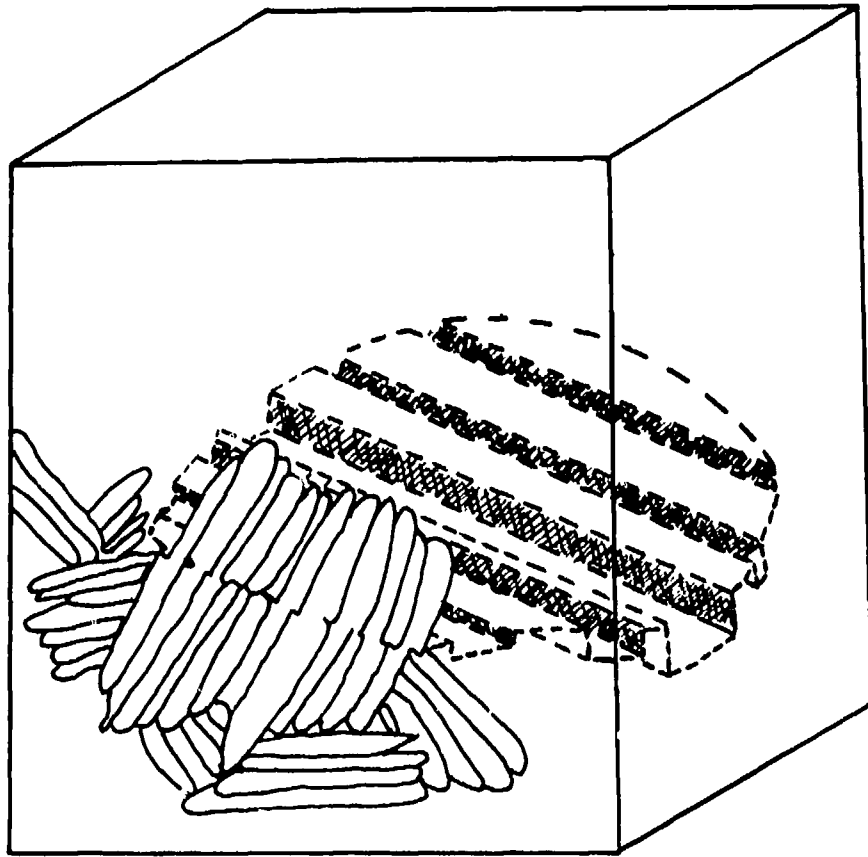


a

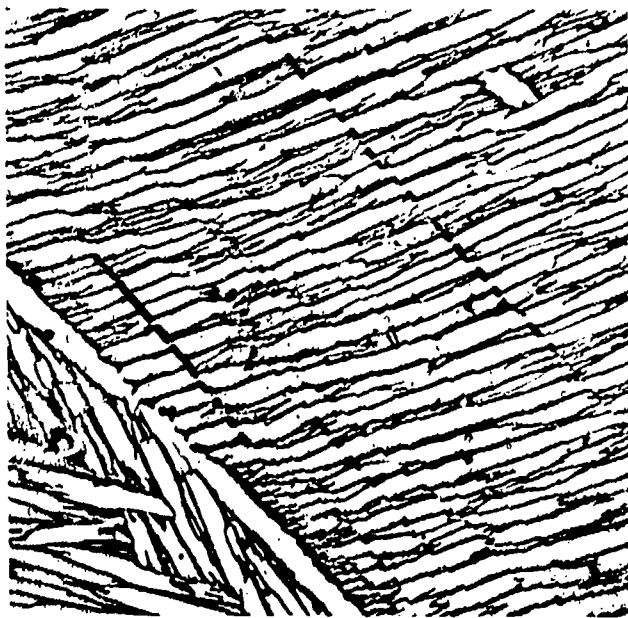


b

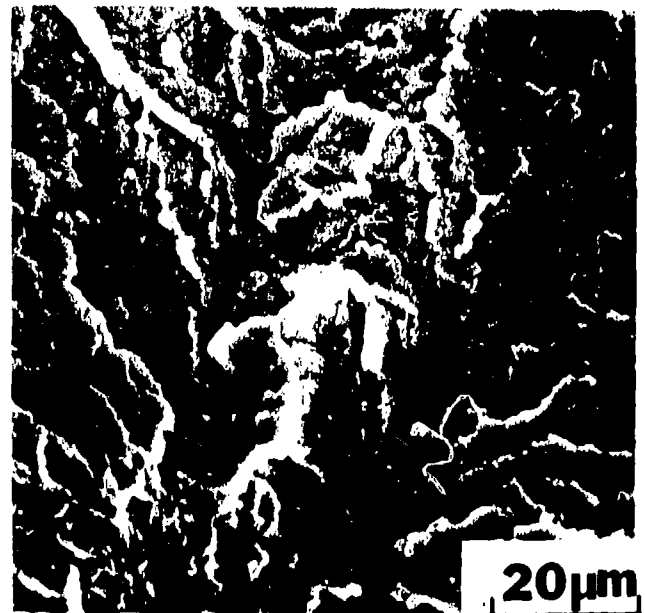
Figure 14



a



b



c

Figure 15

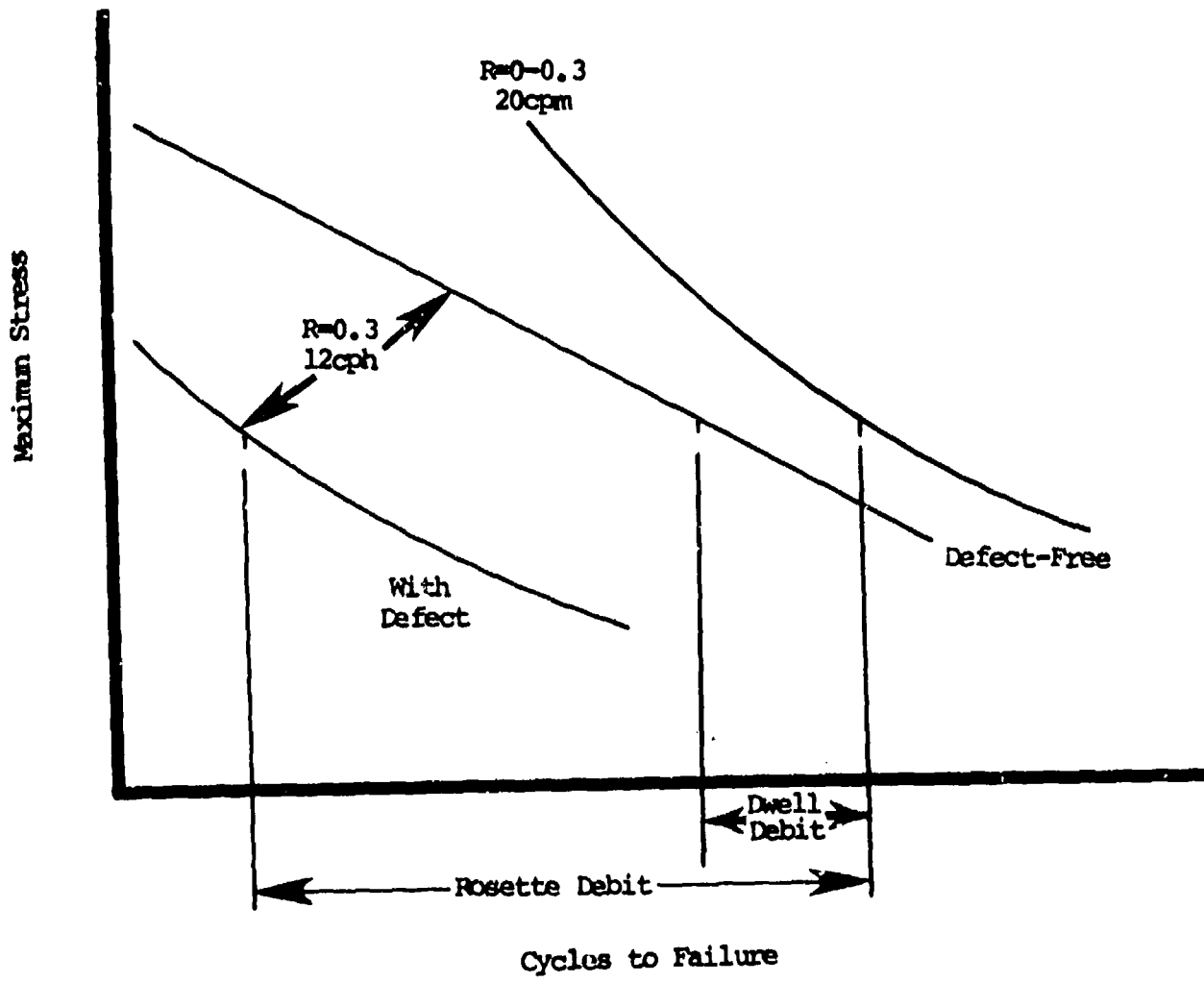


Figure 16

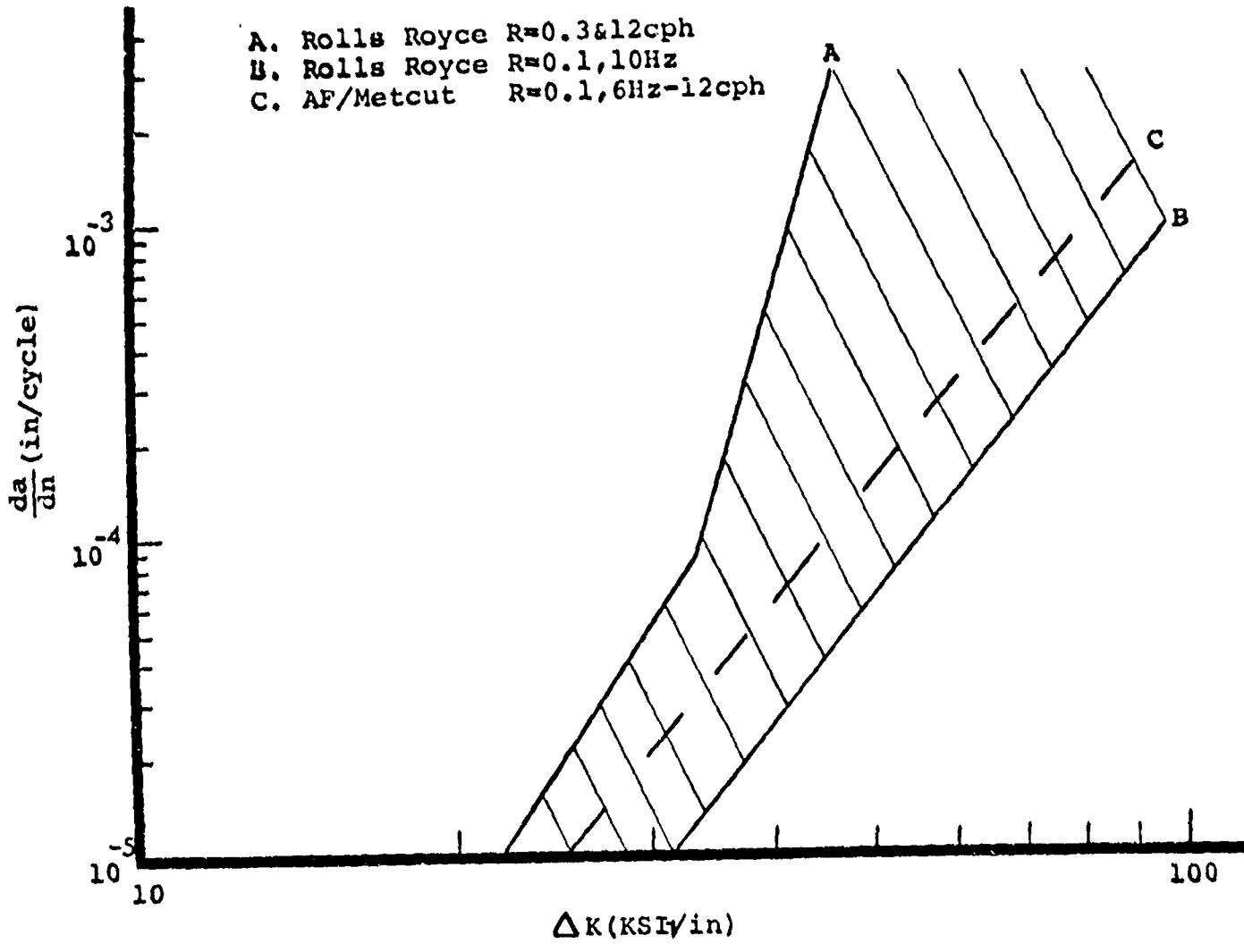


Figure 17

A. Rolls Royce R=0.3&12cph  
C. AF/Metcut R=0.1,6Hz-12cph

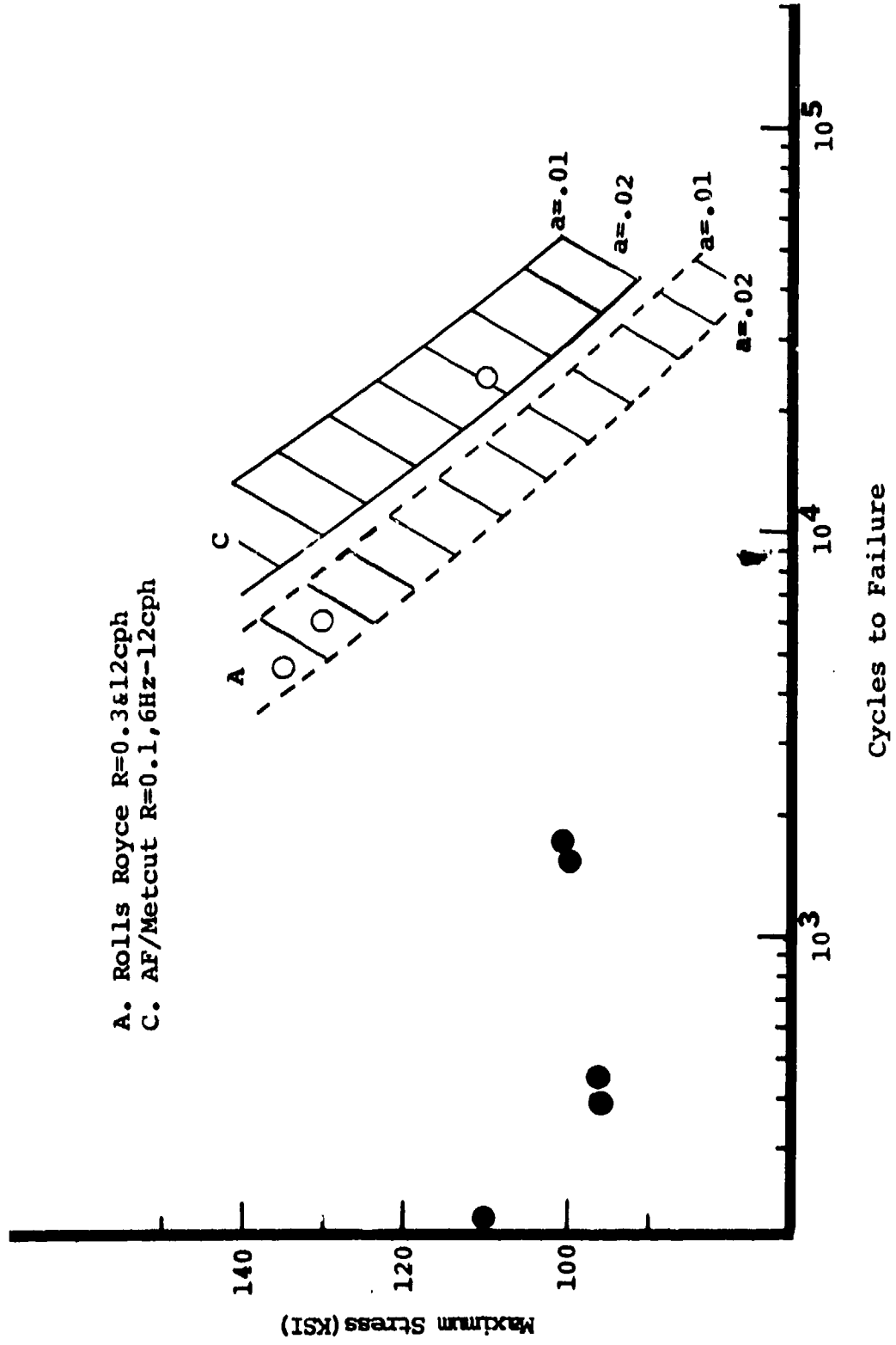


Figure 18

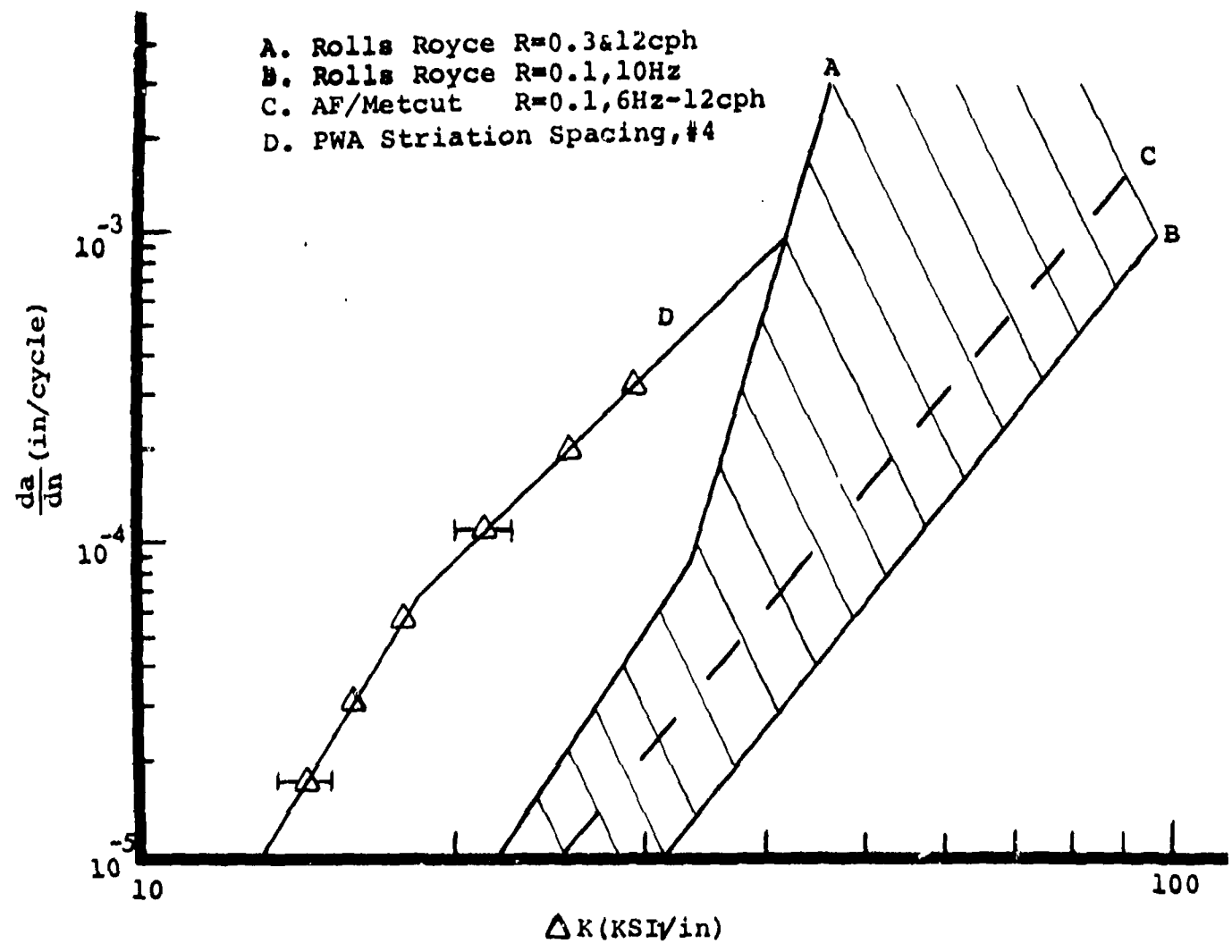


Figure 19

### C. BETA FLECK DEFECTS

#### I. INTRODUCTION

The chemistry and microstructure of  $\beta$ -fleck defects in Ti-6Al-4V were characterized in the earlier part of this investigation and described in detail in the First Annual Report. Tensile and some LCF properties were also reported. It was established that in a stress-relieved condition the presence of  $\beta$ -fleck defects has no effect on crack initiation life during strain-controlled LCF tests at a maximum strain level of 0.9%. This observation applies to material heat-treated differently and to material that was processed differently (billet and forging), although the forged material showed a fatigue debit of a factor of at least two when tested in a as-machined condition. Stress-controlled LCF testing showed the same trend. However, when tested at lower stress levels the  $\beta$ -flecked specimens had longer lives than those without such defects. Further, cracks were observed to nucleate, in all cases studied, at the normal area rather than at the  $\beta$ -fleck defects. From the results it was apparent that the surface conditions (residual stress) must play an important role in the fatigue debit of flecked material. It was also inferred from the crack initiation observations that the presence of  $\beta$ -fleck is symptomatic of a disease rather than the disease itself i.e., the fatigue debit of flecked material may be related to the general microstructure (prior  $\beta$  grain size, secondary  $\beta$  grain size, volume fraction of equiaxed  $\alpha$  particle, etc.) of the flecked material rather than to the details of the  $\beta$ -fleck defect (size, severity, chemistry, etc.).

Against this background, the major effort during this reporting period has been in the study of effects of surface conditions on the stress and strain-controlled LCF properties of Ti-6Al-4V with and without  $\beta$ -fleck defects. Residual stress measurements were made before and after the LCF tests (primarily on strain-controlled half bolt-hole specimens) to determine the effects of microstructures (normal and  $\beta$ -flecked) on relaxation of the surface residual stresses. Determination of compositions at a normal area and a  $\beta$ -flecked area by secondary ion microprobe technique has also been attempted during this reporting period.

#### II. EXPERIMENTAL

##### i. Specimen Fabrication and Testing

Most of the details of the specimen fabrication and testing procedures have been given in the First Annual Report. In addition to LCF testing of specimens with stress-relieved surface,

PRATT &amp; WHITNEY AIRCRAFT

specimens with either as-machined surface or stress-relieved plus glass bead peened surface (12N intensity) were also tested in stress-controlled and strain-controlled modes, the latter has included testing at a lower strain level, 0.7%. To determine the effects of microstructure on surface residual stresses in half bolt-hole specimen machining, three pairs of specimens with different combinations of microstructures in each pair were machined together. The first pair consisted of a specimen with normal microstructure and one with  $\beta$ -flecked microstructure. The second and third pairs consisted of specimens of same microstructures, either normal equiaxed  $\alpha$  microstructure, or  $\beta$ -flecked microstructure.

#### ii. Residual Stress Determination

The residual stress was measured by the two-exposure X-ray diffraction method<sup>(1)</sup> using Cu radiation usually at a setting of 40 KV, 20mA. The angular positions  $2\theta$  of the diffracted beams from (2133) planes were measured at two  $\psi$  angles ( $\psi = 0$  and  $= \pi/4$ ) using a diffractometer which scanned at a constant rate of  $2\theta = 0.1$  per minute. The angular  $2\theta$  shift in the lines upon angular  $\psi$  rotation of the sample with respect to the primary beam was determined by Ogilvie's parabolic fitting method in which five data points are obtained at equal  $2\theta$  intervals about the diffraction peak, and the parabolic curve is fitted by the method of least squares. The residual surface stress is then obtained as a product of the angular  $2\theta$  shift and the stress factor which for Ti-6Al-4V was determined experimentally to be 860 psi per  $2\theta = 0.01^\circ$ .

No correction due to Lorenz polarization and absorption was made since it had been observed that the resulting stress levels were within 1% of those obtained with these correction factors. Beam penetration correction was not made since such correction required the shape of the stress gradient below the surface be known. Without this correction, the calculated stresses appear to be larger and the peak residual stress shifted toward the surface. However, meaningful comparison of results can still be made on a relative basis.

The X-ray measurement by two-exposure technique could only be made on either the fractured or cut half bolt-hole specimens because of the obstruction of the beam by the specimen. A beam of 0.125" wide, 0.5" long was used the latter is parallel to the width of the specimen. On fractured specimens measurements were made as a function of distance from the fractured end which is usually located at the bottom of the bolt hole.

PRATT &amp; WHITNEY AIRCRAFT

Because of the strain gradient on the half bolt-hole gage section the measurements, in effect, yielded information on the residual stresses as a function of cyclic straining, i.e., cyclic surface residual stress relaxation.

### iii. Chemistry Determination by Secondary Ion Mass Spectrometry

A sample from the center of the Ti-6Al-4V billet was taken for analysis. Mass spectra were obtained at a  $\beta$ -flecked band and at a normal area using either  $32O^+$  ions or  $28N^+$  ions after a sputtering of 15 to 30 minutes. The reduction and therefore interpretation of the data are subject to the same limitations described previously in the cleavage rosette studies. To determine the spacial distribution, secondary ion images of V, Fe, O, N, C and H were also taken at the normal and  $\beta$ -flecked areas.

## III. RESULTS

### i. LCF Properties of Ti-6Al-4V

#### 1. Surface Residual Stress Effects

Figure 1 shows strain-controlled crack initiation lives of normal and  $\beta$ -flecked specimens as a function of surface preparations at a maximum strain level of 0.9%. Three different surface conditions had been used; stress relieved and electropolished (SR & EP) which results in no surface residual stress, as-machined and stress-relieving prior to glass bead peening to 12N intensity (SR & GB - 12N). Each data point is an average of two measurements except those of as-machined data points where averages of five measurements per material were given. The bars represent the maximum scatterings in either LCF or residual stress data. As noted previously, in stress-relieved condition there is no difference in the crack initiation life between the normal and the  $\beta$ -flecked materials in either the pancake forging (data indicated by open and filled circles) or the billet (data indicated by open and filled triangles). With increasing surface residual compressive stresses, the crack initiation lives increased in both the normal and  $\beta$ -flecked materials however, that of the former increased faster than the latter. The initiation lives of the  $\beta$ -flecked material are lower than those of the normal material by at least a factor of two in either as-machined or glass-bead peened conditions.

Figure 2 shows the results from stress-controlled LCF tests at a maximum stress of 110 KSI as a function of the same three surface preparations described in the preceding paragraph. The large circles in Figure 2 represent the average lives while the results of individual tests are given by small circles. More scatter in residual stress values and LCF lives is evident for the as-machined condition. However, the same trend as in the strain-controlled tests is observed. Again, fatigue debits in  $\beta$ -flecked material occur only in conjunction with presence compressive surface residual stresses.

## 2. The Influence of Test Conditions

The S-N curves of the  $\beta$ -flecked and normal materials tested in a stress-relieved and electropolished condition are illustrated in Figure 3. The symbols used in this figure have the same meanings as those in Figure 2. At all three stress levels tested, the  $\beta$ -flecked specimens had longer lives than the normal specimens, this difference is larger at lower stress levels. This unexpected observation is confirmed convincingly by the strain-controlled LCF tests at a strain level of 0.7%. The crack initiation results are shown in Table I. It can be seen that the initiation lives of the  $\beta$ -flecked material are longer than those of the normal material by a factor of at least 4 in either WQ or AC heat treated conditions.

### ii. Residual Stress Measurements

The residual stresses measured on the as-machined half bolt-hole specimens are given in Table II. It can be seen that the residual stresses are highly sensitive to microstructures and details of the machining procedures. The residual stresses on as-machined specimens measured after fracture are given in Table III. These measurements were made at locations A, B and C in the order of proximity to the fracture; location C is the closest one to the fracture. As expected the residual stresses decrease toward the fracture (i.e., as the amount of fatigue deformation increases). The important difference between the  $\beta$ -flecked and normal specimens is that residual tensile stresses are developed near the fracture in the former while the residual stresses remained compressive in the latter. Comparing the residual stresses at location A it is obvious that there is large scatter in these data, especially in the  $\beta$ -flecked specimens. As shown in Table II this scatter may be explainable in terms of microstructure and machining details (although all

the specimens were machined using a standard procedure).

### iii. Secondary Ion Mass Spectrometer Measurements

The compositions that were measured after sputtering for 15-30 minutes are given in Table IV. The segregation pattern of the  $\alpha$ -stabilizing and  $\beta$ -stabilizing elements in the normal and  $\beta$ -flecked regions is not clear using this technique. The  $\beta$ -flecked region contains a higher concentration of  $\beta$ -stabilizing Fe and a lower concentration of  $\alpha$ -stabilizing C. On the other hand, the normal region contains higher concentrations of H and Cr both of which are  $\beta$ -stabilizers. The other elements present appear to be due to residual contamination. Some of the secondary ion images are shown in Figure 4. In Figure 4a and b the light areas correspond to the  $\beta$ -phase while the dark areas correspond to the  $\alpha$  phase. It appears from Figure 4b that the change in V concentrations between  $\alpha$  and  $\beta$  phases is a gradual one. Similar observations can be made on Fe (Figure 4c).

## IV. DISCUSSION

The most significant discovery of this study is that the fatigue debit is not caused by the presence of beta fleck defects per se but is rather the result of the interaction of the defect containing microstructure with surface residual stress during fatigue. The defect microstructure not only relax such stresses at faster rate than normal microstructure but originally compressive stresses change sign (to tensile) near the crack initiation sites. It has also been shown that in the absence of residual stresses the fatigue capability of the beta flecked material is equal or superior to normal structure. The advantage of the flecked structures is more clearly evident at lower stresses or applied total strain.

It should also be emphasized that in the stress relieved condition variations in fatigue capability with different processing and/or microstructure are observed. Thus the fatigue results from the forged material are greater than that of the billet and beta heat treatment of the latter material can result in lower fatigue life. Detailed microstructural analyses of these materials will be completed in the next quarter of this contract and will be used to establish if such factors as beta grain size and/or alpha beta interfacial area can be clearly established as the life controlling factor(s). It could be fairly stated that the microstructural trends noted above fit into the general pattern of behavior established for titanium alloys over the past years. Likewise the importance of surface residual stress on fatigue capability has been recognized for some time. However the present investigation

PRATT &amp; WHITNEY AIRCRAFT

attempts to put both these factors together in a systematic way and for the first time attempts to provide insight into why specific behavior patterns are observed.

Accepting the general trends in microstructural relationship to fatigue capability it is still rather unclear why crack origins in the beta flecked material do not nucleate preferentially at these structural discontinuities. This statement may be true of any surface conditions but is probably most applicable to machined or shot peened surfaces. Although not included in the present study crystallographic texture is known to have a pronounced effect on cyclic deformation processes. Indeed reduction in fatigue life of three orders of magnitude has been observed in specific orientations of a textured Ti-6Al-4V product<sup>(2)</sup>. The preferred orientation present in a forged product is usually small compared with sheet or plate. However a local group of grains in an unfavorable orientation (with respect to LCP) may exert an overriding influence on fatigue life. An attempt will be made in the next quarter to establish if texture can account for the location of fatigue crack origins in the material under investigation.

Finally an explanation is required for the mechanism of stress relaxation in these materials. It is inferred that the origin of the decline of surface stresses resides in the interaction of a dynamic set of glissile defects with the applied, and undefined, surface defects. Basic problems in examining defects in half bolt-hole specimens include the large strain gradients imposed on such specimens and the rather small area or volume available for examination. Transmission microscopy will be attempted on samples cut from these specimens in an attempt to elucidate the relaxation mechanism. To supplement this approach a series of flat specimens have been fabricated which will provide a larger area for studying

PRATT & WHITNEY AIRCRAFT

REFERENCES

1. Residual Stress Measurement by X-ray Diffraction - SAE J784a Second Edition August 197, Published by Society of Automative Engineers, Inc. N.Y., N.Y.
2. R.H. Jeal, Private Communication, 1976.

PRATT &amp; WHITNEY AIRCRAFT

TABLE I

CRACK INITIATION LIFE Ti-6Al-4V  
 0-0.007e  
 STRESS-RELIEVED AND ELECTROPOLISHED

<u>Microstructure</u>	<u>Heat Treatment</u>	<u>First Indication</u>	<u>Cycles (10<sup>3</sup>)</u>	
			<u>1/64</u>	<u>1/32</u>
$\beta$ -Fleck Normal	WQ	None at 333 69.0	- 71.0	- 77.0
$\beta$ -Fleck Normal	AC	220.0 50.0	222.0 51.0	226.0 59.0

WQ = 1750°F/1 hr WQ + 1100°F/2 hr AC

AC = 1750°F/1 hr AC + 1100°F/2 hr AC

PRATT &amp; WHITNEY AIRCRAFT

TABLE IISURFACE RESIDUAL STRESSES IN AS-MACHINED Ti-6Al-4V  
HALF BOLT-HOLE SPECIMENS

<u>Half-Bolt Hole Specimen Pairs*</u>		
<u>Number</u>	<u>Microstructures</u>	<u>Residual Stresses (-KSI)</u>
1	Normal	29.6 ± 2.0
	β-Flecked	62.8 ± 8.0
2	Normal	52.0 ± 12.0
	Normal	
3	β-Flecked	25.2 ± 5.2
	β-Flecked	

\*Material α-β pancake forged + 1750°F/1 hr AC + 1100°F/2 hr AC

TABLE III

SURFACE RESIDUAL STRESSES IN AS-MACHINED Ti-6Al-4V  
 HALF BOLT-HOLE SPECIMEN AFTER TESTING

<u>Microstructure (S/N)</u>	<u>No. of Cycles to First Crack Initiation</u>	Stresses (KSI)* at Location		
		<u>A</u>	<u>B</u>	<u>C</u>
$\beta$ - Flecked (9A)	6,000	-2.0	+1.5	+3.0
$\beta$ - Flecked (15B)	7,000	-48.0	-40.0	+12.0
Normal (6A)	19,000	-32.0	-24.0	-17.0
Normal (7A)	25,000	-16.7	-14.5	-1.7

\* + Tensile, - Compressive

PRATT &amp; WHITNEY AIRCRAFT

FIGURE CAPTIONS

1. Fatigue crack initiation lives of normal and  $\beta$ -flecked Ti-6Al-4V as a function of surface preparations. The specimens were tested in strain-controlled LCF at 0.9% $\epsilon$
2. Fatigue live of normal and  $\beta$ -flecked Ti-6Al-4V as a function of surface preparations. The specimens were tested in stress-controlled fatigue at 110 KSI.
3. S-N curves of normal and  $\beta$ -flecked Ti-6Al-4V specimens which were stress-relieved and then electropolished prior to testing
4. (a) 51 V image of a normal area  
(b) 51 V image of a  $\beta$ -flecked area  
(c) 56 Fe image of a  $\beta$ -flecked area

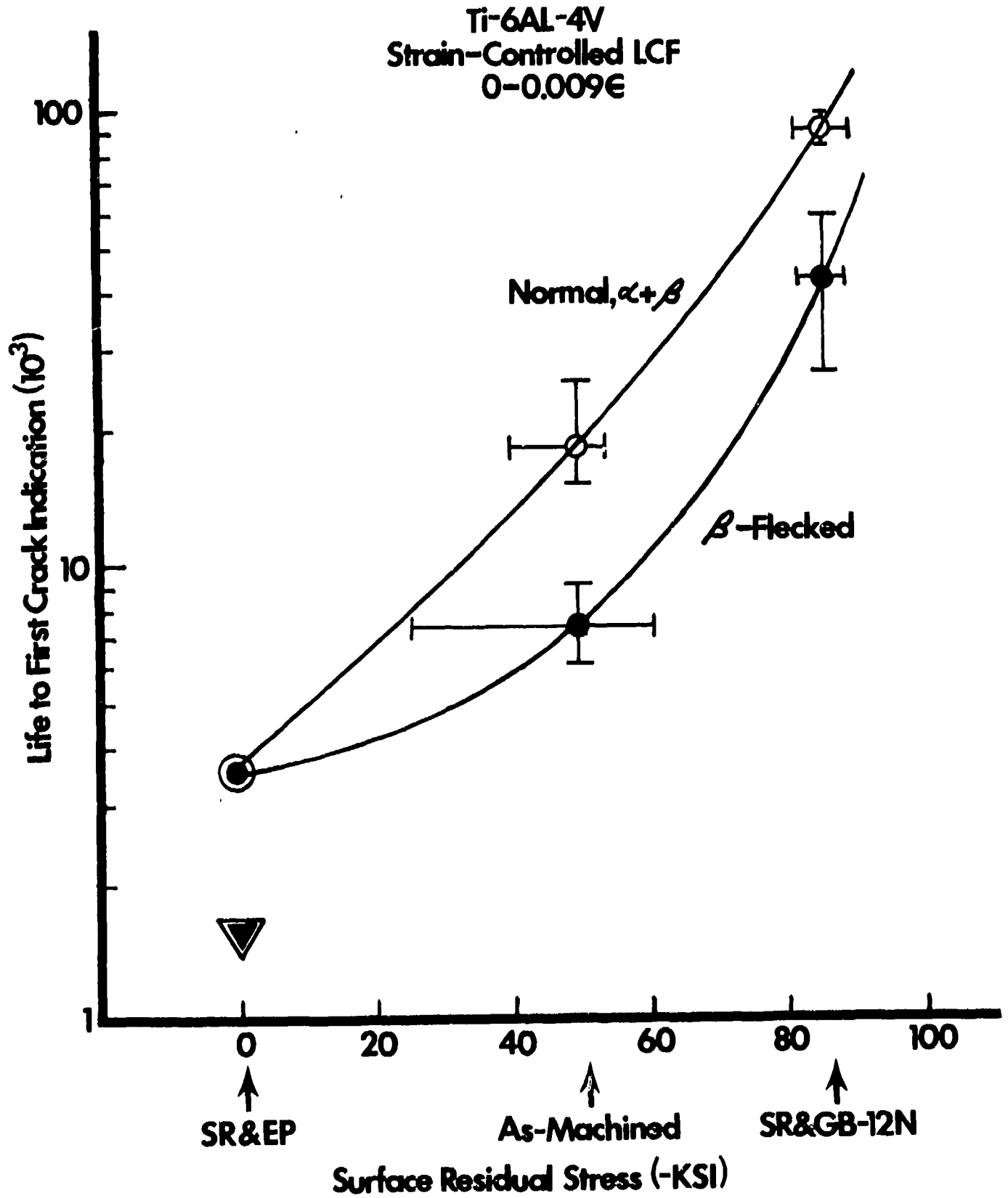


Figure 1

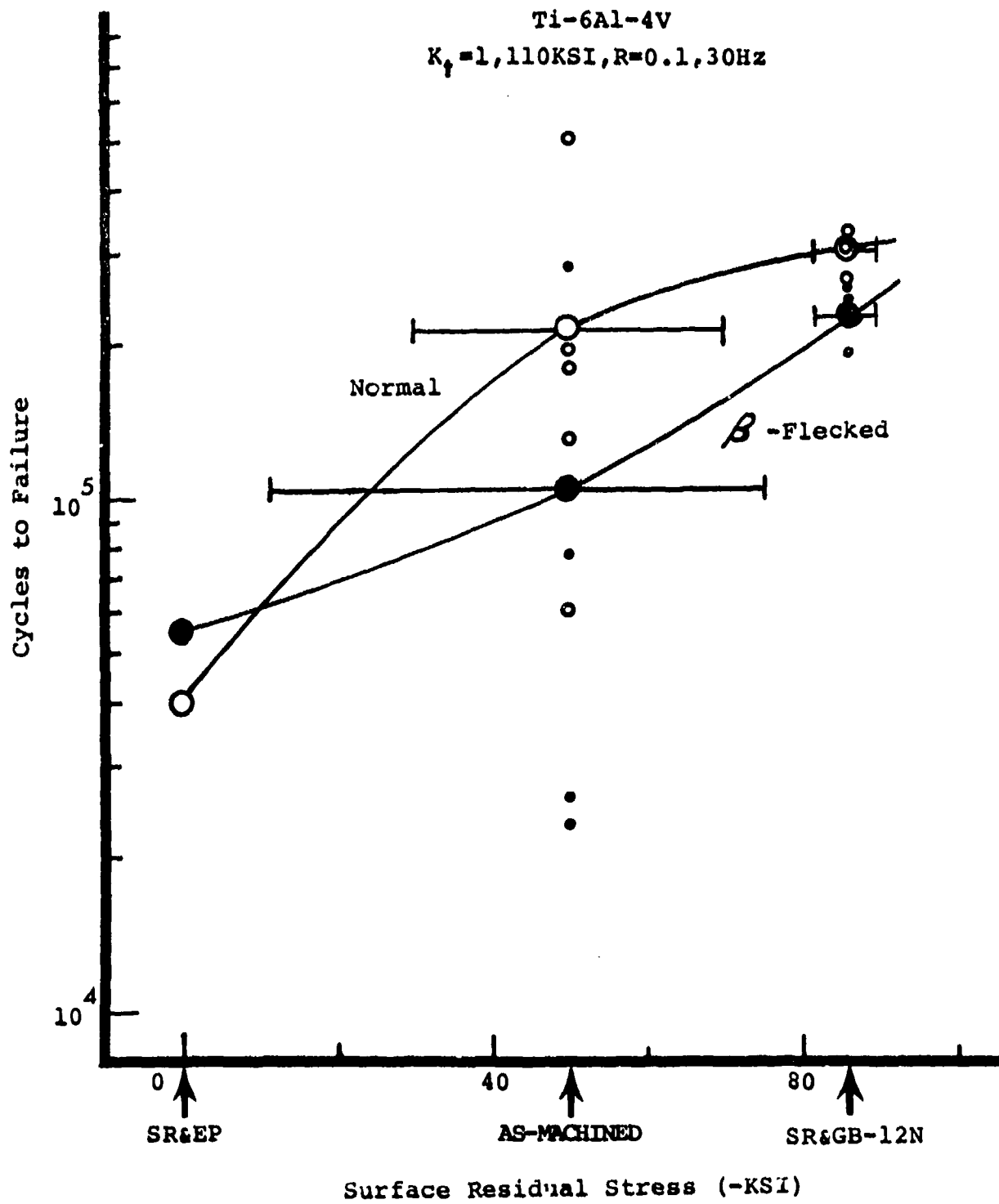
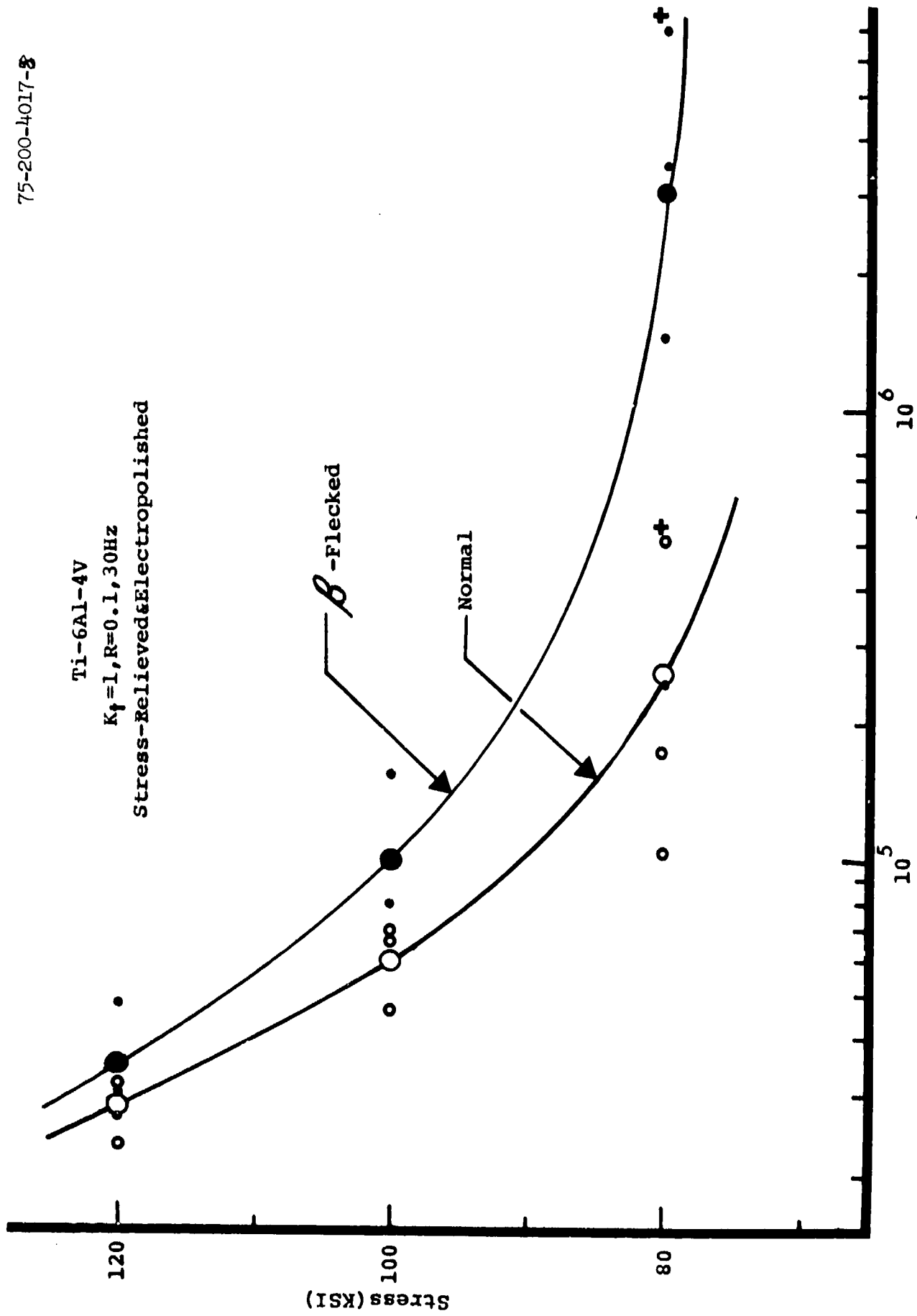


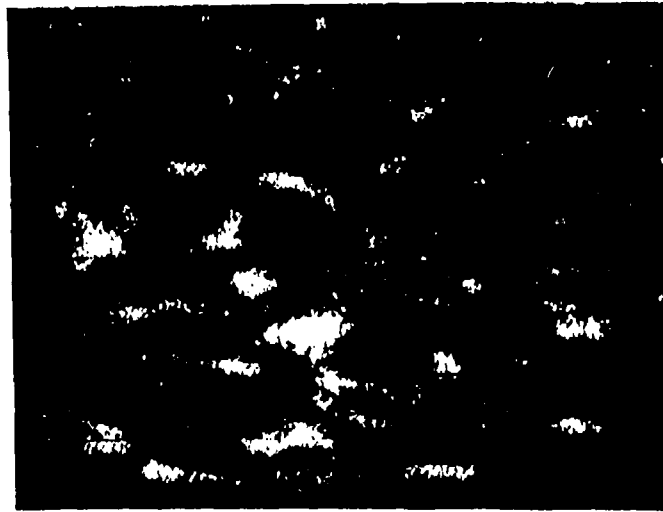
Figure 2

Ti-6Al-4V  
 $K_f = 1, R = 0.1, 30\text{Hz}$   
Stress-Relieved & Electropolished



Cycles to Failure

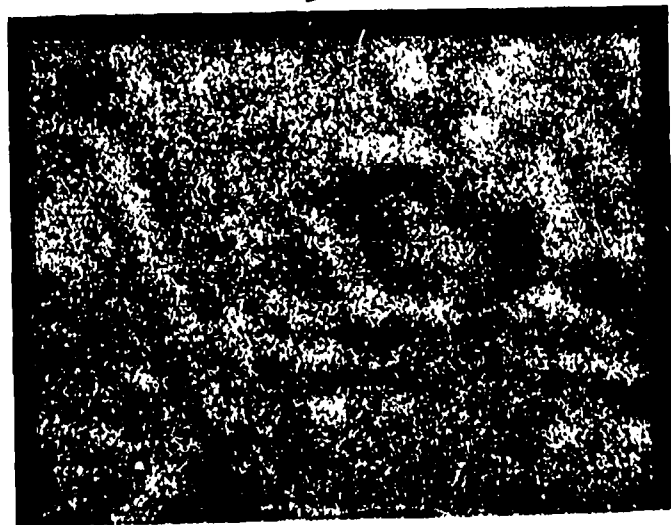
Figure 3



A



B



C

Figure 4